Detailed Analysis of Near Tectonic Features Along the East Pacific Rise at 16°N, Near the Mathematician Hot Spot

M. Le Saout, R. Thibaud, P. Gente

AGU100 ADVANCING EARTH AND SPACE SCIENCE

JGR

Journal of Geophysical Research: Solid Earth

RESEARCH ARTICLE
10.1029/2017JB015301

Key Points:
- The growth of tectonic features differs in response to dike intrusion or brittle extension
- The initiation of brittle extension is strongly controlled by the development of the lithosphere and the dimension of the AML
- There is no significant influence of the Mathematician hot spot on the brittle deformation location but an impact on the deformation intensity

Correspondence to:
M. Le Saout,
mlesaout@geomar.de

Citation:
Le Saout, M., Thibaud, R., & Gente, P. (2018). Detailed analysis of near tectonic features along the East Pacific Rise at 16°N, near the Mathematician hot spot. *Journal of Geophysical Research: Solid Earth*, *123*, 4478–4499. https://doi.org/10.1029/2017JB015301

Received 22 DEC 2017
Accepted 18 MAY 2018
Accepted article online 24 MAY 2018
Published online 6 JUN 2018

Detailed Analysis of Near Tectonic Features Along the East Pacific Rise at 16°N, Near the Mathematician Hot Spot

M. Le Saout[1,2], R. Thibaud[3], and P. Gente[1]

[1]Laboratoire Géosciences Océan, UBO/UBS/CNRS, IUEM, Plouzané, France, [2]Now at Geomar Helmholtz Centre for Ocean Research, Kiel, Germany, [3]École Navale, IRENav, Brest, France

Abstract Spreading processes at the axes of fast spreading ridges are mainly controlled by magmatic activity, whereas tectonic activity dominates further away from the axis. High-resolution near-bottom bathymetry data, photographs, videos, and human observations from submersible surveys are used to develop a detailed tectonic analysis of the 16°N segment of the East Pacific Rise (EPR). These data are used to evaluate how a highly magmatic segment, close to a hot spot, affects the nucleation and evolution of faulting patterns and impacts the evaluation of tectonic strain within 2 km of the spreading axis. Our study shows that (1) the growth of tectonic features differs in response to dike intrusion and tectonic extension, (2) the initiation of brittle extension is strongly controlled by the location of the axial magma lens and the development of layer 2A, and (3) the high magmatic budget and the off-axis magma lens in the west part of the plateau do not significantly impact the initiation of brittle extension along the central portion of the 16°N segment. Within the axial summit region, more than 2% of plate separation at 16°N on the EPR is accommodated by brittle extension, as is observed at other EPR segments. The interaction of the Mathematician hot spot with this EPR segment has no significant influence on the initiation of the tectonic deformation, but it does reduce the development of the brittle deformation.

1. Introduction

Mid-ocean ridge morphology results from the interaction between tectonic and volcanic activity and is influenced by the internal structure of the lithosphere. While a tectonically active region could extend to at least 40 km from the axis (Alexander & Macdonald, 1996), most of the interactions impacting ridge morphologies occur within a relatively narrow area around the ridge axis. On the East Pacific Rise (EPR), the spreading process is commonly associated with a narrow axial summit trough (AST), ranging from 5 to 10 m deep and up to 200 m wide (e.g., Chadwick & Embley, 1998; Cormier et al., 2003; Fornari et al., 1998; Soule et al., 2009). Most lavas erupted along the AST are flowing down the slope of the axial high, resulting in a thickening of seismic layer 2A (presumed to be this extrusive lava layer) of ~200 to ~500 m within 1–2 km from the AST (e.g., Carbotte et al., 1997; Hooft et al., 1996; Vera & Diebold, 1994). This thickening of the extrusive layer is also affected by faulting and ponding of lava flows against fault scarps (Escartín et al., 2007).

Numerous studies described in details the interaction between tectonic and magmatic activity at the axis linked to the formation of the AST. Many studies suggest that the ASTs form from dike intrusions that induce fissures and faulting (e.g., Carbotte et al., 2006; Chadwick & Embley, 1998; Cormier et al., 2003; Haymon et al., 1991; Mastin & Pollard, 1988; Pollard et al., 1983; Rubin, 1992; Rubin & Pollard, 1988; Soule et al., 2009). Along the EPR, narrow ASTs are assumed to form above dike intrusions. They are readily buried by subsequent lavas flows, contributing to the overall relief of the volcanic ridges. The waning magmatism results in the collapse of calderas or subsidence of the axial seafloor and contributes to the widening of the AST through ongoing intrusion and diking, with less voluminous volcanic eruptions being confined by the graben walls (e.g., Fornari et al., 1998; Lagabrielle & Cormier, 1999; Soule et al., 2009). If those studies investigate the formation of ASTs and the deformation associated with them, only a few describe the evolution of this deformation away from the AST. Nevertheless, Soule et al. (2009) and Escartín et al. (2007) propose that tectonic deformation is generally underestimated due to the burial of faults by lava flows. If even a small part of the tectonic extension on the EPR at 9–10°N is accommodated within a narrow zone, extending 2 km from the AST, then Escartín et al. (2007) suggest that more than 75% of the faults in this zone would be either partially or totally buried by lava flows. Comparison of faulting in areas with recent magmatic overprinting

to areas with older lava flows shows that the determined levels of tectonic deformation and associated strain are approximately 5 times lower in the younger regions versus the older magmatic regions (Escartín et al., 2007). Therefore, we would expect to see a similar underestimation of tectonic activity from the areas of recent magmatic overprinting along the 16°N segment, compared to the regions with older magmatic activity. These determinations are based on observations of detailed tectonic and volcanic features using near-bottom high-resolution bathymetry and other highly detailed observations. These kinds of data and observations are a key factor in revealing tectonic and volcanic process (e.g., Chadwick et al., 2013; Clague et al., 2014; Deschamps et al., 2007; Escartín et al., 2007; Ferrini et al., 2007; Soule et al., 2009).

Away from the ridge axis, some studies have focused on the initiation of the off-axis extensional faulting (Carbotte et al., 1997; Garel et al., 2002; Lagabrielle et al., 2001; Macdonald, 1998; Macdonald et al., 1996) and the built of lateral grabens along fast spreading ridges. Previous studies show that the initiation of extensional faulting occurs at distances between 600 and 4,000 m from the axis (e.g., Fornari et al., 1998; Garel et al., 2002; Macdonald et al., 1996; Searle, 1984; Wright, Haymon, & Fornari, 1995; Wright, Haymon, & MacDonald, 1995). Closer to the axis the lithosphere is assumed to be too thin, weak, and hot to sustain shear failure (e.g., Carbotte & Macdonald, 1994b) and fractures are instead associated with the development of an AST or tensional cracking (Carbotte & Macdonald, 1994a; Crowder & Macdonald, 2000; Perfit & Chadwick, 1998). Analog modeling (e.g., Lagabrielle et al., 2001) indicates that this off-axis deformation is controlled by a combination of deflation of a magma lens and regional extension. Thus, the magmatic supply to the ridge plays an important role in the location of the initiation of the brittle deformation. A series of bathymetric profiles perpendicular to the EPR ridge axis have confirmed those observations (Garel et al., 2002) and show that the broader the axial cross sectional is, the further away from the axis the brittle deformation initiates. However, only a few microbathymetric studies have been focused on the deformation formed close to the morphological axis (Deschamps et al., 2007; Escartín et al., 2007) and none of these studies were undertaken in an environment with high magma budget supplied by a hot spot. Indeed, the interaction between mid-ocean ridges and hot spots typically influences the thermal state and magma supply of the ridge (e.g., Christie et al., 2005; Detrick et al., 2002; Ingle et al., 2010). As a consequence, this interaction is reflected in the resulting thickness of the crust, morphology of the ridge axis, lava morphology, and the structure of the underlying lithosphere (Canales et al., 2002; White et al., 2008) and should also impact the location of the initiation of brittle deformation.

We present a detailed tectonic analysis of the 16°N segment of the EPR using near-bottom microbathymetry, photographs, videos, and direct visual observations made from a submersible. These detailed analyses extend the morphological descriptions presented by Le Saout et al. (2014). These new data allow us to evaluate the small-scale interactions between volcanic and tectonic processes near ASTs, the nucleation and evolution of faulting patterns, and the distribution of tectonic strain in the context of an unusual spreading segment influenced by a hot spot. We estimate the distribution and dimensions of tectonic features and make distinctions between fractures associated with eruptive features and those not associated with magmatic features. We propose two origins for the nucleation and/or evolution of fractures around the 16°N AST and define relationships between fractures, lava flows, and off-axis changes in the internal structure of the lithosphere, that is, a change in the thickness of the seismic layer 2A and a volume change of the magma lens.

2. Geological Context

2.1. Morphological Segmentation

The 16°N segment of the EPR, located between 15°25′N and 16°20′N, north of the Orozco fracture zone (Figure 1), has a spreading rate of ~85 mm/year (Weiland & Macdonald, 1996). It is the broadest and shallowest segment of the entire northern EPR with an unusually prominent along-axial-ridge, up to 15 km wide at its base and up 750 m high with respect to the adjacent abyssal hills (e.g., Baker et al., 2001; Carbotte et al., 2000; Carlut et al., 2004; Le Saout et al., 2014; Scheirer & Macdonald, 1995; Weiland & Macdonald, 1996). This morphology has been attributed to the influence of a hot spot (e.g., Carbotte et al., 2000; Carlut et al., 2004; Scheirer & Macdonald, 1995; Weiland & Macdonald, 1996), named "Mathematician hot spot" (Le Saout et al., 2014; Mougel et al., 2014, 2015). A relationship between these features is supported by (1) the presence of the Mudskipper volcanic seamount ridge, located less than 5 km away from the ridge axis, on the western flank of the 16°N axial rise (e.g., Baker et al., 2001; Carlut et al., 2004; Macdonald et al., 1992; Weiland &

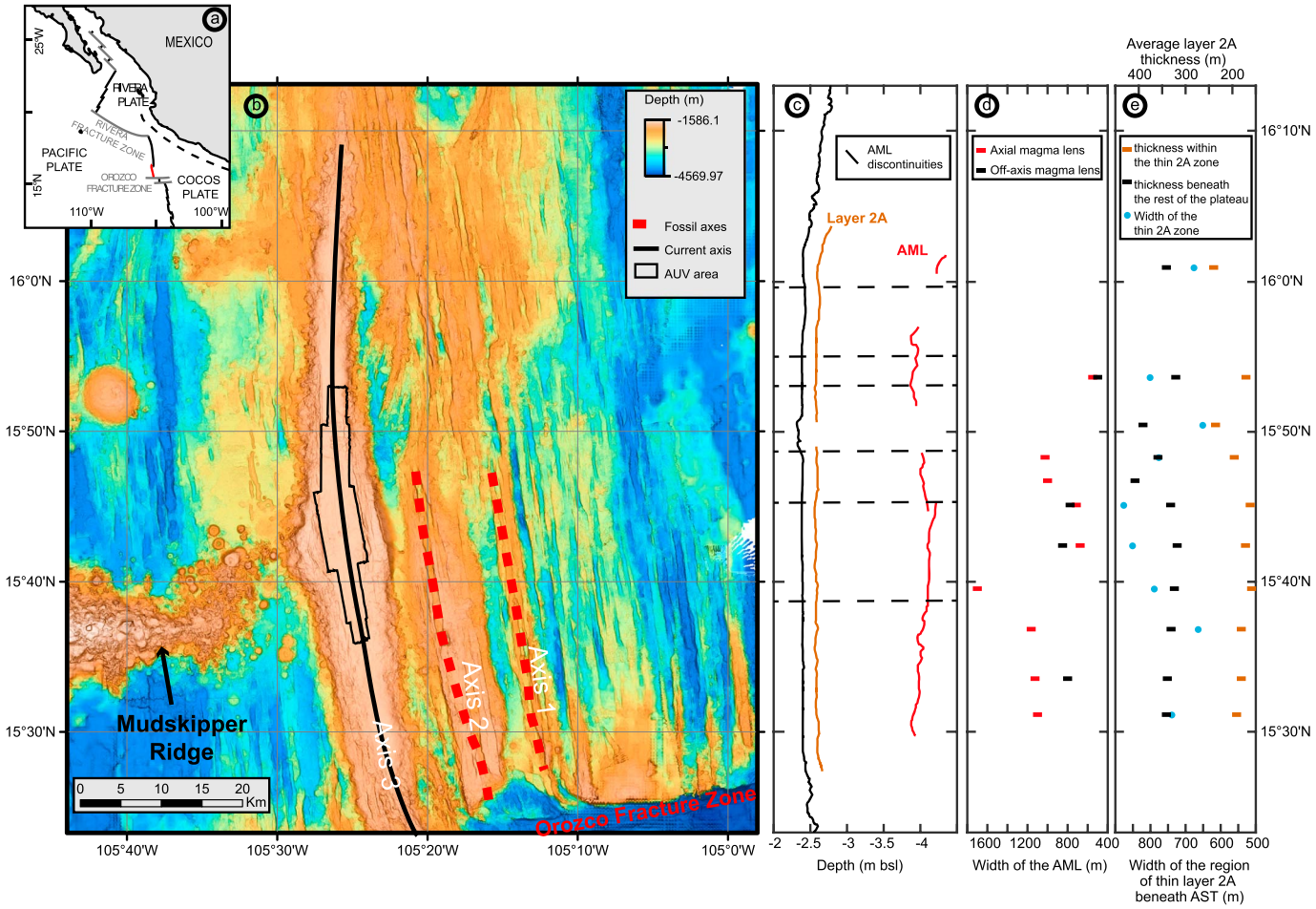

Figure 1. (a) Location of the 16°N East Pacific Rise segment (in red). (b) Bathymetric map of the 16°N segment, with the Mudskipper Ridge, the present ridge axis (Axis 3) and two fossil axes (Axes 1 and 2). Area of near-bottom AUV bathymetric survey (black box) is shown. (c–e) Plots showing the geometry of layer 2A and the magma lenses inferred by seismic profiles along and across the axis (Carbotte et al., 2000): (c) along-axis variation of the seafloor (black line), layer 2A (brown line) and depth of the axial magma lens (AML; red line). Locations of AML discontinuities are indicated by dashed lines. (d) Widths of the AML (red squares) and the off-axis magma lens (black squares) versus latitude. (e) Plot of the layer 2A characteristics within the axial region. The width of the thin layer 2A zone is indicated by blue circles. The thickness of layer 2A is indicated by brown squares within the thin 2A zone and by black squares beneath the rest of the plateau.

Macdonald, 1996); (2) the location of the shallowest part of the dome, at 2,200 m depth, near the projected intersection of the Mudskipper volcanic chain with the ridge axis (15°42′N); (3) a geochemical anomaly identified in the axis-lavas that indicates a mixing between a MORB and a more enriched and heterogeneous source associated with the hot spot magmatism (Mougel et al., 2014, 2015); and (4) the presence of extinct spreading axes east of the ridge axis, indicating at least two westward jumps of 7 and 9 km in the direction of the hot spot at 150 and 300 kyr (e.g., Carbotte et al., 2000; Shah & Buck, 2006; Weiland & Macdonald, 1996). Carbotte et al. (2000) proposed that the 16°N segment became established in its present position 85 to 105 kyr ago, corresponding to the isochron located between the axial rise and oblique abyssal hills in the east.

Between 15°36′N and 15°53′N, based on data from Macdonald et al. (1992) and Carbotte et al. (2000), and on high-resolution bathymetry and videos (the same used in our present study), Le Saout et al. (2014) identified six 4–9.5 km long third-order spreading segments referred as subsegments (Figure 2). These subsegments are characterized by 10 distinct well-defined ASTs of variable depth (1 to 40 m) and width (10 to 1,000 m). The subsegments are defined by discontinuities at 15°37′N, 15°41′N, 15°45.5′N, 15°48′N, and 15°51′N, and these discontinuities are either lateral offsets (by 200–600 m), abrupt variations of the geometry of the ASTs (width and depth), or changes in the trend (by up to 5°) of the ASTs. Morphological discontinuities also often correlate with discontinuities of the axial melt lens (Le Saout et al., 2014).

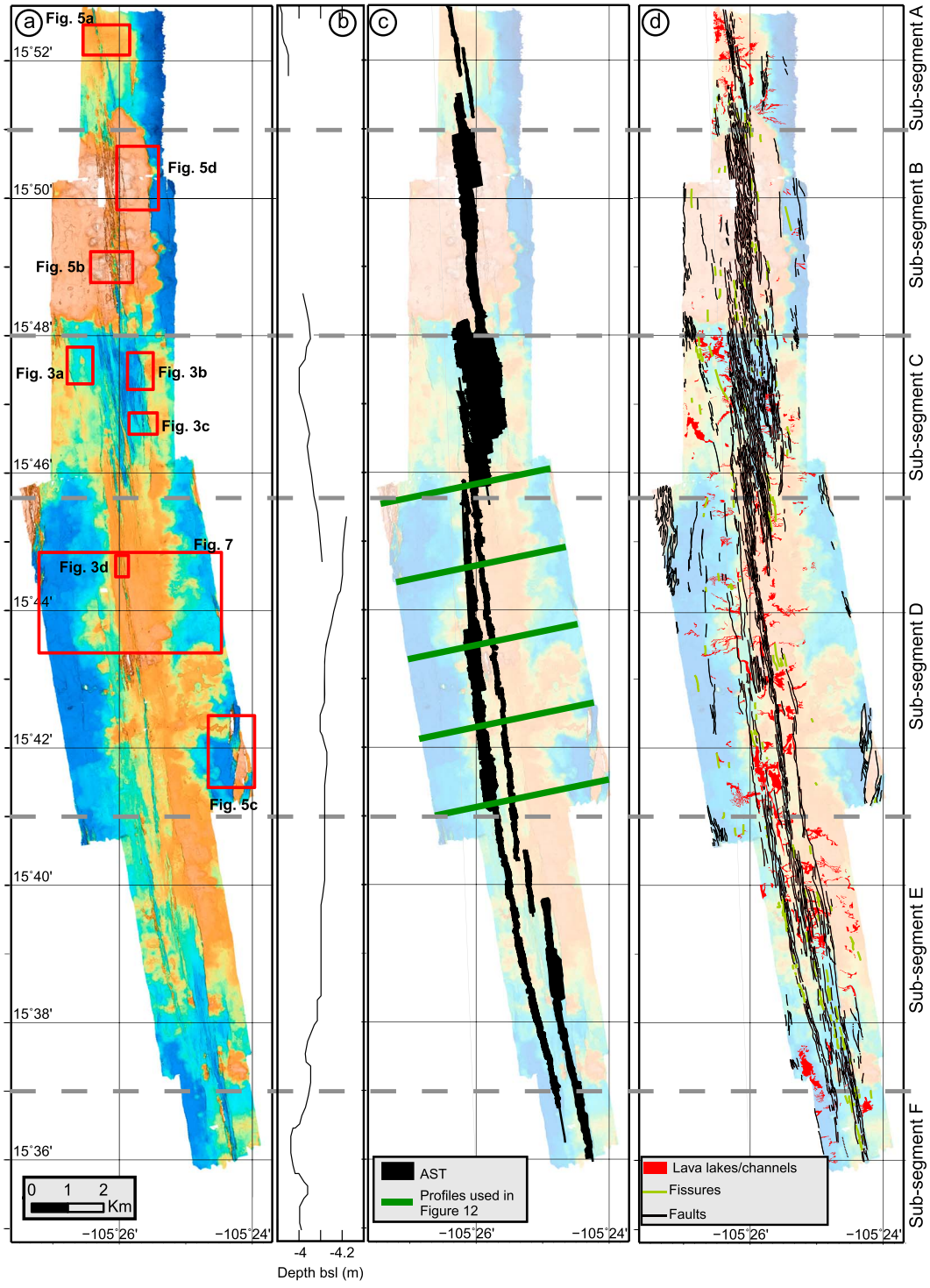

Figure 2. (a) Microbathymetric map (1 m grid cell size) of the 16°N segment (East Pacific Rise). Third-order segmentation of the summit plateau is indicated by grey dashed lines. The close-ups illustrating in Figures 3, 5, and 7 and located by red boxes. (b) Depth of AML below sea level from Carbotte et al. (2000). (c) Axial summit troughs (AST) are indicated in black on the microbathymetry. The bold green lines on subsegment D indicate bathymetric profiles used to measure the tectonic strain (on Figure 12). (d) Structural map based on analysis of video and high-resolution bathymetric data, including faults (black), fissures (green), and lava channels (red).

These subsegments present distinctive lava morphologies which include pillows, lobates, collapsed lava lakes, and inflated sheet flows (Deschamps et al., 2014; Le Saout et al., 2014), with the proportion of each facies varying from one third-order segment to another. Some subsegments are dominated by one lava type (e.g., lobate flows for subsegments A and C or pillow flows for subsegment B), while others do not have predominant facies (e.g., similar proportions of lobate and pillow flows for subsegments D and E). Gregg and Smith (2003) and McClinton et al. (2013) proposed that lava flow morphologies are related to the underlying slopes; however, in our study area, the slope (ranging from 0.5 to 1.5°) is insignificant. Therefore, it is more likely that the observed variations in volcanic types reflect variations in effusion rate (e.g., Fink & Griffiths, 1998; Gregg & Fink, 1995) and/or are related to distinct magmatic sources.

2.2. Crustal Structure of the 16°N Segment

On the 16°N segment, a previous seismic study (Carbotte et al., 1998, 2000) defines the crustal structure under the ridge axis (Figures 1c–1e) and identifies the locations and dimensions of the magmatic lenses and of the extrusive layer 2A. The roof of the axial magma lens (AML) is located at a depth of 1,300–1,500 m under the ridge crest (Figure 1c). The AML is observed along almost the whole length of the segment, but there are some discontinuities where the lens disappears, deepens, or is more difficult to detect (Carbotte et al., 2000). These locations coincide with the third-order morphological discontinuities mentioned above and are observed at the following locations: (1) near 15°37′N, the reflector of the AML is weak and disrupted; (2) between 15°48.6′N and 15°51.8′N and the AML is not observed; and (3) north of 15°45′N, the AML seismic reflector is shifted by 100 m to a shallower depth. At about 15°41′N, there is no clear evidence of a discontinuity in the AML seismic reflector between subsegments E and D. Nevertheless, subsegment D contains an off-axis magma lens, located about 1.2 km westward, that is not evidence along the others segments. Carbotte et al. (1998, 2000) also evidenced the seismic layer 2A, which is 107 ± 45 m thick and ~750 m wide under the ASTs in the axial summit plateau (Figure 1e). Between 100 and 300 m further away from the ASTs, the thickness of the layer 2A increases rapidly, to reach a thickness of ~ 350 m underneath the rest of the summit plateau. Le Saout et al. (2014) noted no relation between the AST dimensions and AML or layer 2A features, which suggests that AST morphological variations do not reflect major changes in the internal structure of the ridge. Instead, Le Saout et al. (2014) propose that AST morphology is related to changes in eruptive volcanic activity, and ASTs would widen with the decline of the eruptive activity.

3. Data, Terminology, and Methods

3.1. Data

The present study is based on surface bathymetry, near-bottom microbathymetry, and submersible dive photographs and videos collected during the PARISUB cruise. Surface bathymetry was collected using the *R/V L'Atalante* SIMRAD EM122 hull-mounted multibeam echo sounder. The gridded data set from this survey covers a region of about 5,700 km^2 with 40-m resolution (Figure 1) and 10-m resolution over the axial summit plateau. Microbathymetric data were collected using a SIMRAD 2000 multibeam echo sounder (CNRS/GéosciencesAzur) fitted to the AUV *Aster-X*. The AUV was operated at a height of 70 m above the seafloor, along 200-m-spaced lines, for a total of 720 km and 110 hr. Microbathymetric data used in this paper are available from the NAUTILUS portal (http://campagnes.flotteoceanographique.fr/campagnes/10010020/). These data were combined to produce a digital elevation model with a 1-m grid spacing. The resulting microbathymetry covers an area of about 120 km^2 (4 km across axis by 30 km along axis) from 15°36′N to 15°53′N and from 105°24′W to 105°27.5′W, on the central part of the summit plateau (Figures 1 and 2). Photographs and videos from the seafloor complete the data set (Le Saout et al., 2014) and were acquired across the summit plateau from 12 dives using the manned submersible *Nautile* (Ifremer), providing observational ground truthing to interpreting the bathymetric data.

3.2. Terminology

We use the term "fracture" from the classic terminology used in structural geology, describing a planar discontinuity in a rock formation that formed in response to an applied stress field. The three types of fractures discussed in this study (fissures, faults, and hybrid fractures) are defined as follows. "Fissure" refers to an extensional fracture whose walls have opened significantly in a direction normal to the plane of the fracture. Morphologically, these fissures are composed of two closely spaced facing scarps with a relatively similar length and height, forming a V-shape in cross section (Figure 3a). In this study, we digitized these fissures

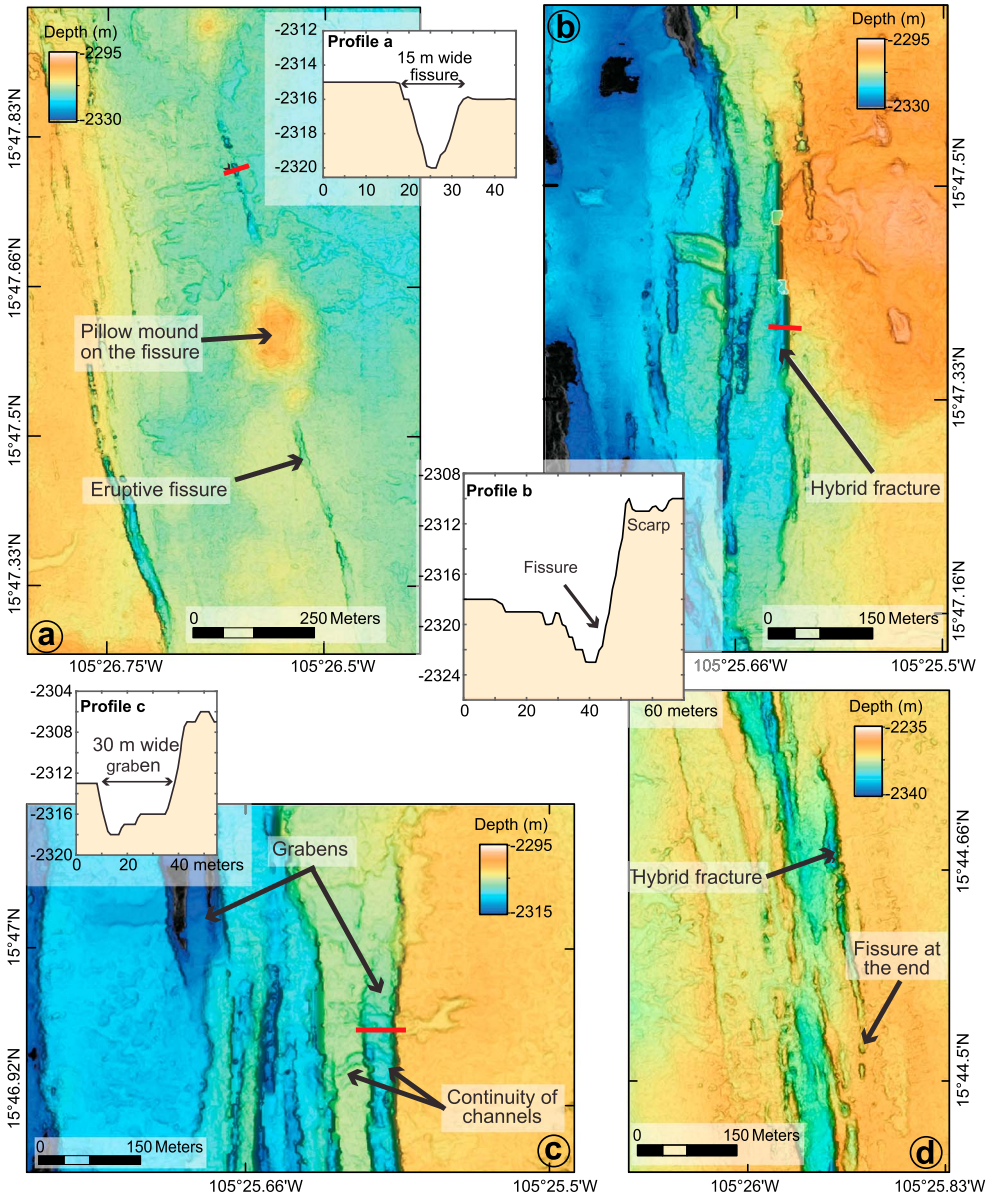

Figure 3. (a through d) Sample microbathymetric maps illustrating the different fracture geometry. The close-ups are located in Figures 2 and 6. (a) Eruptive fissure composed of two facing scarps, closely spaced, that meet at their base. The eruption along the fissure as result in a pillow mound located directly on top of the fissure. (b) Hybrid fracture that displays a vertical throw with an extensional fissure at the bottom of the scarp. (c) Graben consisting of two facing vertical scarp that cut through previous lava channels. (d) Hybrid fracture with fissures at its extremities. This relation indicates that hybrid fracture observed here evolved from a fissure.

by following their centerlines. "Faults" are here defined as fractures associated with a shear motion perpendicular to their surface, resulting in a vertical displacement across them. When not covered by lava flows or talus, fault scarps expose truncated lava sections (Figures 4a and 4c), and they often consist of several linked segments. Faults are digitized following the crests of the fault scarp, defined as a sharp change in the slope between the seafloor and the top of the scarp (Figure 4b). The bottom of the fault scarp is also defined as a sharp change in the slope between the scarp and the seafloor at the base of the fault. "Hybrid fractures" display both extensional and shear motions and show vertical throw with an extensional fissure at the bottom of the scarp (Figures 3b and 3c). The tips of hybrid fractures often have a fissure-like morphology indicating a variation of the deformation along the fracture (Figure 3d). Hybrid fractures correspond to a transitional form, where the initial fissure then evolves into a fault (e.g., Deschamps et al., 2007; Ramsey & Chester, 2004) with constraint only focused on one side of the fracture. They are digitized in the same way as for faults, following the crest of the higher scarp.

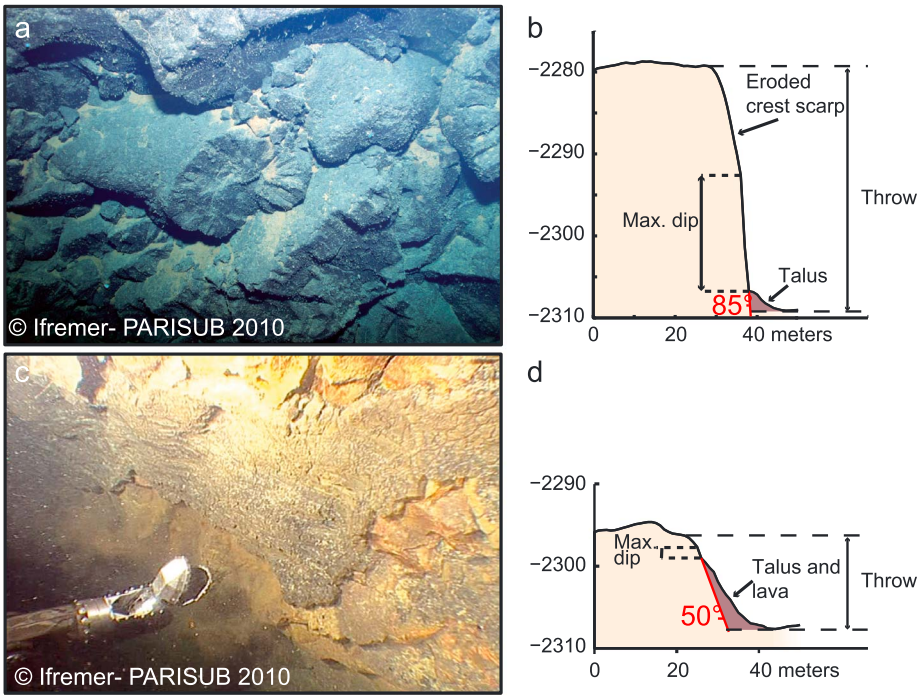

Figure 4. (a) Steep scarp (85°) exposing former pristine lava sections and not covered by subsequent volcanic products. (b and d) Bathymetric cross section illustrating how vertical throw and maximum dip is measured. (c) Fault scarp with horizontal selvages forming during the progressive drainage of lava lakes, resulting in a low dip of the initial scarp. Photos acquired by submersible Nautile during the PARISUB cruise in 2010.

Lava channels and lava lakes are typically observed in lobate flows and result from the collapse of a solidified lobate crust after subsequent drainback (e.g., Embley & Chadwick, 1994; Fink & Fletcher, 1978). When they are located on the flank of the eruptive fissure, lava channels are elongated collapse structures that reflect the principal direction in which the lava was flowing. Within the AST and on its edges, they are usually perpendicular to the ambient stress. Along the 16°N segments, those collapse structures are about 0.5–2 m deep (Le Saout et al., 2014).

3.3. Methods

Fracture dimensions (i.e., vertical throw and dip of faults and width and depth of fissures) are measured using a series of microbathymetric profiles perpendicular to the fracture. On a fracture profile, the throw is defined as the height difference between the crest and the bottom of the scarp, as has been used in previous studies (Figures 4b and 4d; e.g., Bohnenstiehl & Carbotte, 2001; Carbotte et al., 2003; Cowie, 1998; Deschamps et al., 2007; Escartín et al., 2007).

Errors in the measurements are directly associated with the methods of acquisition (either perpendicular or parallel to the fractures), the data resolution (1 m), and the manual digitization of the fractures. We estimate that the horizontal error derived from the 1 m data resolution is probably on the order of ±1 m, and the vertical error is estimated to be less than 0.5 m. The dip error has not been calculated for this data set but a previous study, with similar data resolution (Deschamps et al., 2007), estimates that the error associated with the dip is often lower than 6°. The determination of the fissure depth has the largest error due to the acquisition method and the inability to the signal to reach the maximal depth of the fissure, especially in the case of narrow fissures. Furthermore, fractures generally display variable displacement along strike. Commonly, the vertical displacement on the fracture reaches its maximum at the midpoint of the fault and decreases toward the extremities. In some cases, the measured vertical displacement is more variable along strike, which may result from the growth of faults by linkage (e.g., Cowie, 1998) or from their partial coverage by lava flows (e.g., Bohnenstiehl & Kleinrock, 2000; Deschamps et al., 2007). The dip of a scarp also varies due to erosion of the scarp crest, or its coverage by slope talus or lava flows (e.g., Carbotte et al., 2003; Deschamps et al., 2007; Figure 4). As a consequence, the measured dip value corresponds to the apparent dimensions of the fracture but not its real dimensions. Generally, the combination of the different sources of error results in an

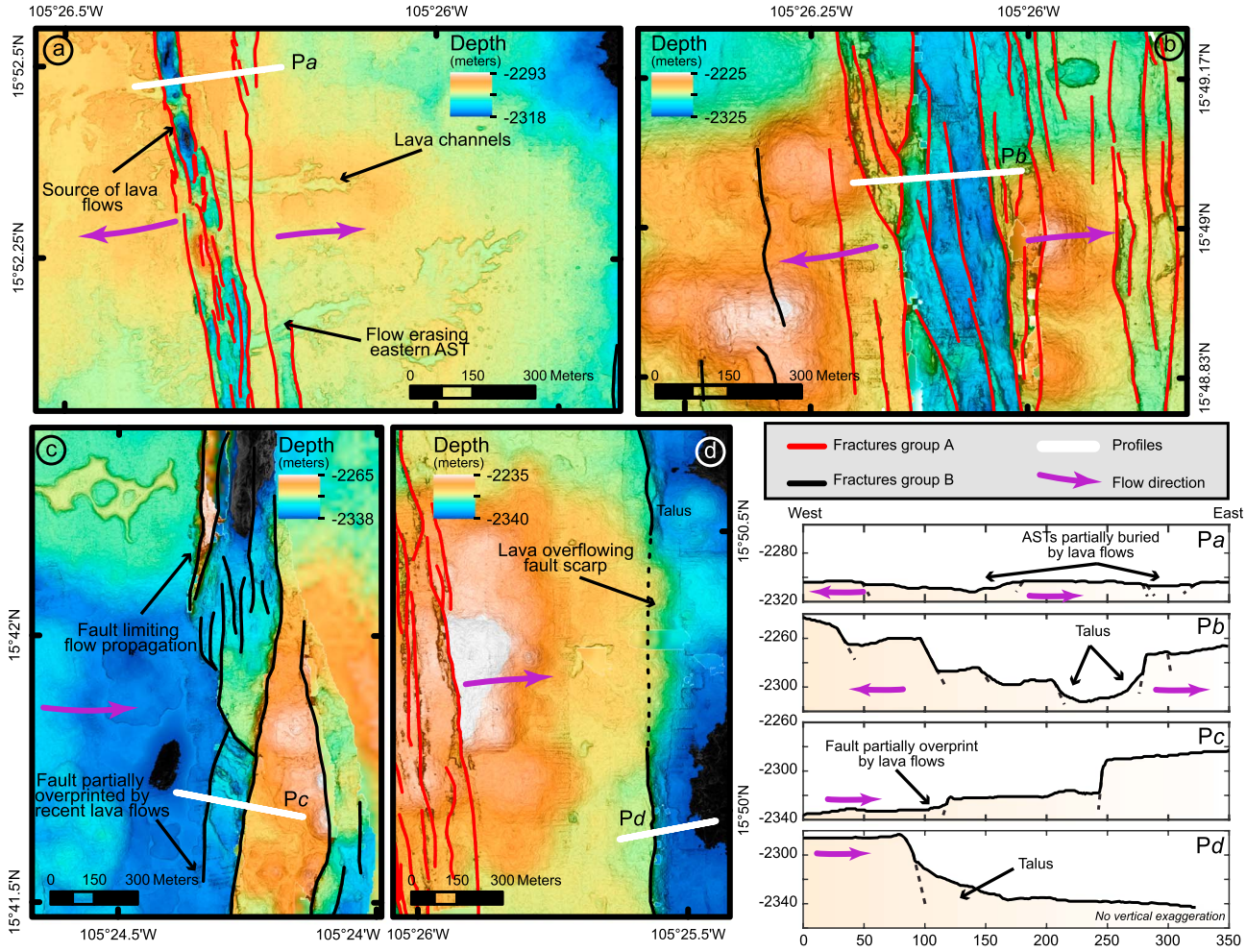

Figure 5. (a–d) Sample microbathymetric maps illustrating the different types of deformation. The close-ups are located in Figure 2a. The cross sections displayed in the lower right of Figure 5 are indicated by thick red lines (P*a*–P*d*) in the maps. Fractures are highlighted by red (group A) or black (group B) lines, and the lava flow direction is shown by purple arrows. (a) Fractures located at a center of lobate flows with divergent flow fronts and channels. (b) Fractures located at the center of pillow flows with divergent flow fronts on both sides of the axis. (c) Fractures located on the side of the summit plateau. They are facing the flow fronts and limit lava flow propagation. (d) Fractures located on the eastern side of the AST are cutting through some older flows and are partially erased by a younger lava flow.

underestimation of the fracture parameters. Thus, for the whole area, only the maximum values for each individual fracture are employed.

Taking into account the faulting patterns that can be extracted from the microbathymetry, we determined the fracture distribution in this region using cell width of 140 m. This cell width was chosen to give the best resolution for the fracture distribution, with respect to the observed average distance between fractures (see section 4.2.). We study the distribution of two parameters: (1) the cumulative fracture length, where each value corresponds to the sum of the length of each fracture segment in the cell, independently of their type (i.e., fissures, hybrid fractures, or faults), and (2) the mean dip, where each value corresponds to the mean of the maximum dip of each fault or hybrid fracture within the cell.

4. Observations

4.1. Relation Between Fractures and Lava Flows

Detailed analysis of lava flow distributions and identification of their sources allows us to distinguish two tectonic contexts. The first corresponds to fractures located at the starting point of a lava channel in lobate flows and/or are centered within lava flows with divergent flow fronts on each side of the fracture (Figures 5a and 5b and profiles P*a* and P*b*). The second corresponds to fractures not associated with lava channel or flow axis

(Figures 5c and 5d and profiles P*a* and P*b*). Scarps either face the ridge axis (inward facing faults, e.g., profile P*c* in Figure 5) or face away from the axis (outward facing scarps, e.g., profile P*d* in Figure 5). If the relation between fracture and eruptive processes varies between the two contexts, in both, fractures are often modified by lava flows. Figure 5a and profile P*a* show that fractures located in a highly volcanic context appear to be almost completely covered by lava flows resulting in a relatively flat area. In other regions, fractures can serve as dams for lava flow propagation (Figure 5c), and their vertical trough are partially (profile P*c*) or totally covered by the lava flows (Figure 5d).

For the next, even if a strict classification is not established, the relationship between fractures and eruptive centers is used to make a distinction between fractures associated with lava flow eruption (named group A) and fractures not associated with lava flow eruption (named group B).

4.2. Fracture Distribution

In this study, 792 fractures are mapped across the whole area (Figure 6a) with an average density of 2.2 km/km^2. However, the fracture distribution is not homogeneous and the spacing between fractures varies from 11 to 1,008 m with an average value of 140 m (choose as cell size for the density calculation). The fracture density map (Figure 6b) shows that the fracture distribution varies both along and across the ridge axis, with the maximum variation in fracture distribution observed across the ridge axis. Indeed, fractures are preferentially located at the ridge axis (~60%) with a density of up to 39.5 km/km^2, and they delimit the location of the ASTs. Outside the ASTs, fractures exist but they are less abundant (usually less than 8 km/km^2) and are more scattered. This study also shows an asymmetry in the fracture distribution with respect to the current axis (Figure 7). The clearest example is observed on the central and broadest part of the ridge axis (between 15°41′N and 15°46′N, which corresponds to the subsegment D), with a lack of fractures over a distance of 2.3 km on the eastern side of the axis. On the western side of the summit plateau in subsegment D, lava flows are limited by inward facing scarps, which delimit a second parallel AST (Figure 7). Looking at the across-axis distribution of fractures in function of their relation to eruptive sources, the fracture in the group A are focused within or in the close proximity to the ASTs (less than 600 m away). They represent 73% of all the identified fractures. The fractures in the group B are observed away, more than 755 m from the spreading axis, and they are more abundant on the edge of the plateau (~83% of group B), where the lava flows have been dated at 2–3 ka (Carlut et al., 2004).

Along the ridge axis, the distribution and geometry of the fractures are also highly variable between segments, with subsegments B and C showing the strongest variations. Subsegment C is characterized by a higher fracture density (usually higher than 14 km / km^2) compared to the other subsegments where the fracture density is usually lower than 14 km/km^2 (Figure 6b). Subsegment B presents similar fracture density to subsegment C but the fractures are characterized by larger dips, usually higher than 70° (Figure 6c), whereas along the rest of the ridge, dips are usually lower than 65°. These two extreme subsegments are also thought to contain older lava flows (2 ± 1 kyr) compared to regions with a narrow AST (e.g., subsegments A and D) where paleointensity analyses indicate lava ages from tens to hundreds of years (Carlut et al., 2004). The results of Carlut et al. (2004) are supported by our visual observations obtained from the Nautile dives. In subsegment B, fractures also expose truncated lava sections with no evidence of later coverage by volcanic flow on their scarp (Figure 4a). This suggests the absence of lava posterior to the deformation that could have filled the AST before collapsed as observed in subsegment D (Figure 4c). In subsegment C, fractures are observed cutting through older lava flows, and lava channels are vertically offset by these fractures, delimiting 20- to 60-m wide grabens (Figure 3c and associated profile).

4.3. Fractures Characteristics

Fissures, hybrid fractures, and faults identified using the microbathymetry correspond to 15.5%, 5.5%, and 79% of the total fractures, respectively. Due to the resolution of our data, we assume that fissures or hybrid fractures with a horizontal displacement smaller than 3 m are not identified. In addition, the proportion of hybrid fractures compared to faults is probably also underestimated, due to the presence of talus at the foot scarps or more recent lava flows that could have filled the extensional fissures. However, fissures and hybrid fractures are numerous both within and on the edges of the ASTs, as revealed by the Nautile dives videos. Typically, the mapped fissures and hybrid fractures vary from 3 to 25 m in width, with a depth lower than 10 m.

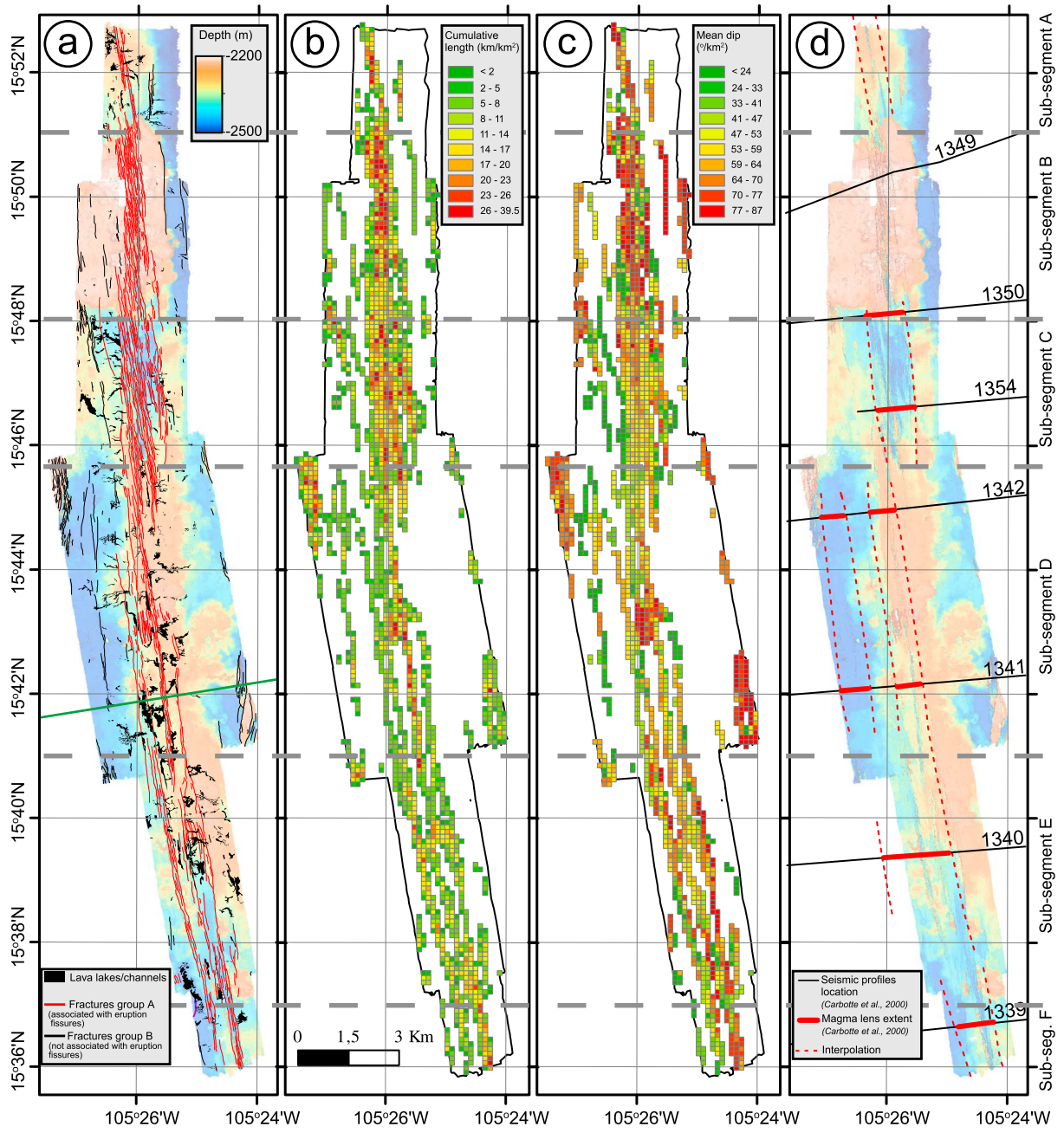

Figure 6. (a) Structural map of the EPR 16°N segment indicating fractures (faults, hybrid fractures, and fissures) from group A (red lines) and group B (black lines). The lava channels and lakes (from Le Saout et al., 2014) are shown in black. The green line shows the bathymetric profile of Figure 11. (b) Graphic representation of the cumulative length of the fractures in 40 km^2 cells. (c) Graphic representation of the mean scarp dips in 40 km^2 cells. (d) Map of illustrating the horizontal extension of the magma lens. The data issue from the seismic profiles (Carbotte et al., 2000) is indicated by a bold red line along the profiles; the interpretation of the horizontal extent between profile is indicated by a dashed red line.

The dips and vertical throws of faults and hybrid fractures display a large range in values (Figures 6, 8, and 9). Dips vary from 20° to 87°, with a more frequent dip of 62° for group A and between 63 and 72° for group B (Figure 8b). Vertical throws vary from 0.7 to 80 m, with throws lower than 10 m for most fractures in both groups (Figure 8c). The relationship between dip and vertical throw is displayed in Figure 8d and shows an exponential relationship, where scarps with smaller throw (<10 m) are characterized by a wider range of dip (20° to 80°), whereas scarps with throw higher than 10 m have dips greater than 50°. Even taking into account maximal dips and throws, these values are still often underestimated (e.g., Bohnenstiehl &

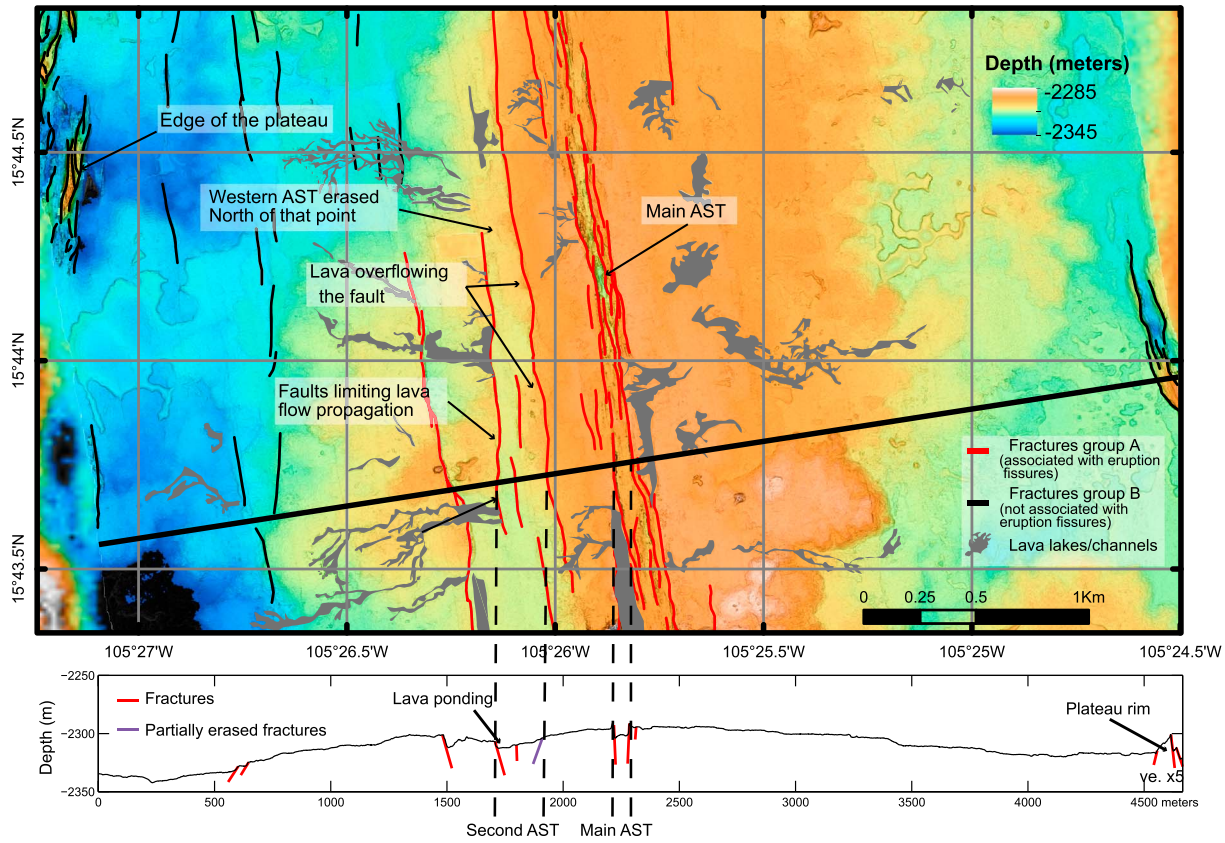

Figure 7. High-resolution bathymetry (1 m-grid-cell size) showing the asymmetry of the relief on both sides of the central axis. No tectonic features appear on the eastern side of the central axis, while several are identified on the western side. A large second AST (black dashed lines) on the western side of the ridge axis accounts for the observed asymmetry. Fractures are indicated in red (group A) and black (group B) on the map. Lava channels and lakes from Le Saout et al. (2014) are indicated in dark grey. The figure is located in Figure 2a.

Kleinrock, 2000; Carbotte et al., 2003; Deschamps et al., 2007). Indeed, the *Nautile* dive videos in the study area reveal that particularly low apparent fault dips (i.e., $<40°$) result from partial of total coverage of fault scarp by lava flows (as displayed, for example, by horizontal selvages on some fault scarps, reflecting different lava lake levels during drainback) or from both erosion of the top and presence of talus at the bottom of fault scarps (Figures 4b and 4d) that distort completely the measure of the dip. These observations are especially true for scarps with smaller throw values (<7 m) that have higher probability of having their original dip underestimated.

Previous studies show that cumulative size-frequency distribution of fault parameters, in the form of cumulative frequency versus fault scarp height or fault length plots, can provide constraints about the regime of deformation (e.g., Ackermann et al., 2001; Ackermann & Schlische, 1997; Bohnenstiehl & Carbotte, 2001; Bohnenstiehl & Kleinrock, 1999; Bonnet et al., 2001; Carbotte & Macdonald, 1994b; Cowie et al., 1993, 1995; Deschamps et al., 2007). Four regimes have been identified by this cumulative size-frequency distribution method. The "nucleation regime" in an early stage of deformation is characterized by an exponential law distribution. In the "growth regime," the fractures are characterized by an increase of their vertical throw and show a power law distribution. The "coalescence regime" corresponds to the lengthening of the fractures by coalescence and interaction of adjoining fractures, and is identified by a distortion of the power law distribution, which follows an exponential distribution for the longest fractures. Higher levels of strain may result in a "saturation regime" where fractures stop to interacting with each other and became proportionally spaced. In this regime, the cumulative size-frequency follows an exponential distribution (Deschamps et al., 2007). As less than 75% of the 120 fractures from group B are entirely mapped, we cannot base our study on fracture lengths, and therefore, we used the cumulative size-frequency versus vertical throw plot to yield information about the regime of deformation.

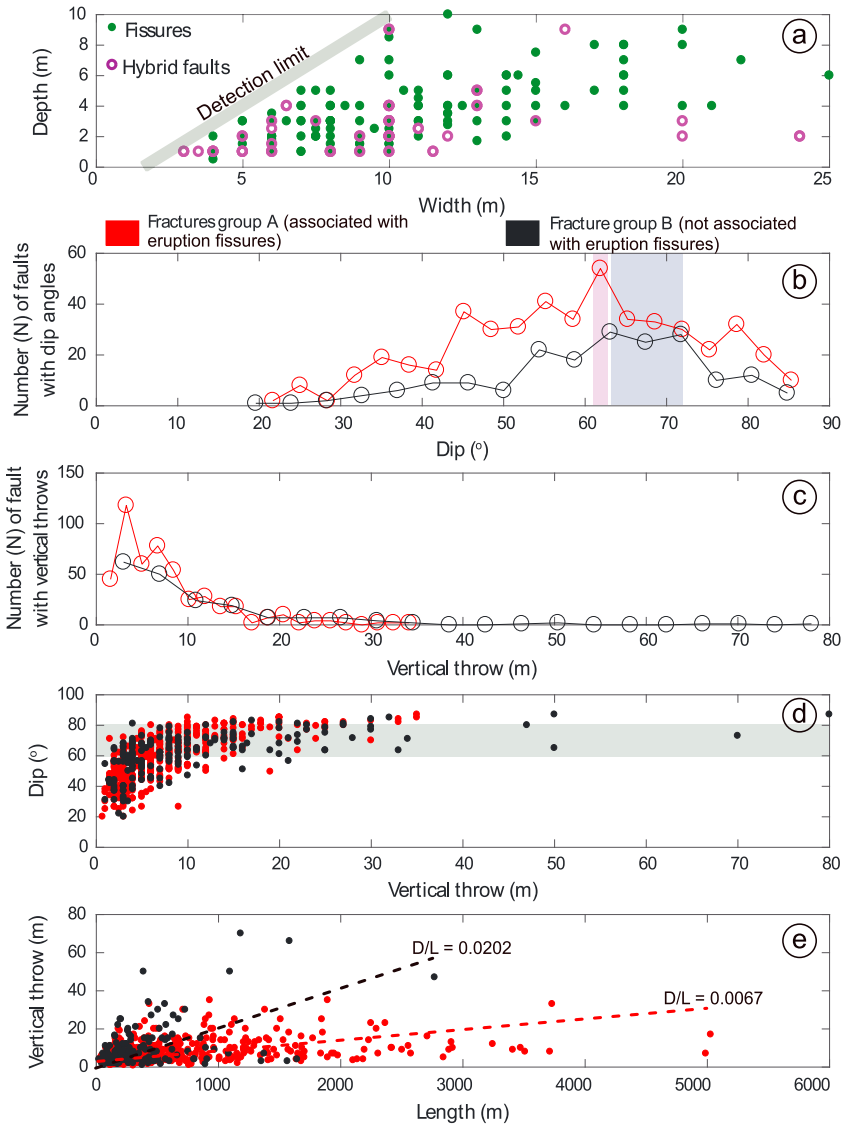

Figure 8. (a) Fissures (green dots) and hybrid fractures (purple circles) depth versus width along the EPR 16°N segment. The gray line indicates the limit of the data resolution. For Figure 8b, the group A fractures are shown by red circles, and the group B fractures by black circles. (b) Frequency of the maximum apparent fault dips. For both populations, the most frequent dips are highlighted by the blue (group B) and purple (group A) vertical boxes. (c) Frequency of the maximum apparent vertical throws on the fractures. (d) Dip versus vertical throw diagram. The grey area corresponds to the most common dip values for fractures not affected by volcanic deposits or erosion processes. (e) Fault lengths (L) versus vertical throws (D) measurements from 618 faults and hybrid fractures entirely map. The D/L ratio for fractures from groups A and B are indicated.

Figure 9 shows a maximum vertical throw versus cumulative frequency log-log plot, using 669 faults and hybrid fractures. The line fit was determined using regression of the data comparing linear logarithmic and exponential equations. The fault scarps used for this statistical analysis mainly follow an exponential distribution (Figure 9). However, scarps with higher vertical throw do not plot on an exponential trend and instead follow a power line fit (Figure 9). The transition between the exponential and power distributions is not sharp but seems to encompass vertical throw ranging from 10 to 20 m.

To determine whether our population of faults follow either a power or exponential distribution, we analyzed the cumulative size-frequency distribution based on (1) eastward and westward dipping faults (Figure 10a) and (2) fracture groups A or B (Figure 10b). Eastward and westward facing faults have a relatively similar abundance (329 and 340 fractures, respectively; Figure 10a). Both follow an exponential

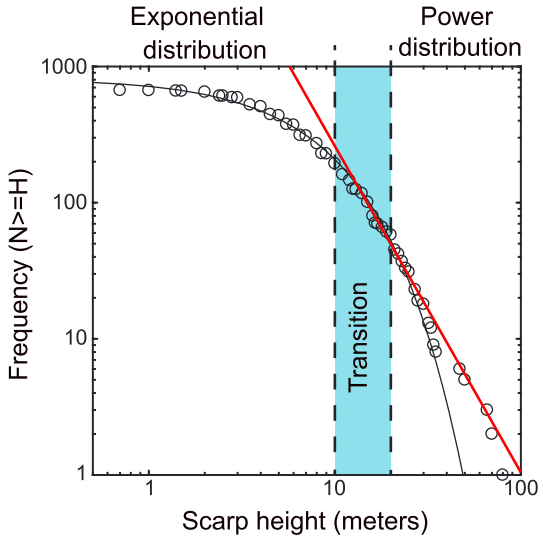

Figure 9. Cumulative frequency maximum height (H) log-log plot for 669 faults and hybrid fractures (*N* = number). An exponential line fit is shown in black, and a power law line fit is shown in red. The area of transition between exponential and power distribution is shown in blue.

distribution, with a fitting equation of $y = 400.6e^{-0.1362x}$ with a $R^2 = 0.996$ for group A and $y = 422.6e^{-0.1394x}$ with a $R^2 = 0.997$ for group B. The exponential line fit exponent values for the two population of fractures (−0.1362 and −0.1394) are very similar, suggesting that fault scarp growth is independent of the direction in which the fault scarps face.

In contrast, the study based on fault group shows that fractures in groups A and B have contrasted line fit exponents (−0.1488 and −0.1085, respectively; Figure 10b). For fractures in group A, the vertical throws follow an exponential distribution ($y = 602.2e^{-0.1488x}$, with $R^2 = 0.994$). However, for the group B we can distinguish a transition from exponential ($y = 218.6 * x^{-0.1085}$, with $R^2 = 0.997$) to power law distribution ($y = 6415.7 * x^{-1.8372}$, with $R^2 = 0.988$). As previously noted, the transition from exponential to power law distribution is observed for vertical throw values ranging between 10 and 20 m high.

5. Discussion

The combined analysis of high-resolution bathymetry and submersible dive photos and videos provides constraints on (1) the nucleation and evolution of fault patterns and (2) on the origin of the deformation. The variability of the shallow crustal structures derived from seismic reflection data provides additional information on the possible relationship between crustal deformation, magma reservoir dimensions, and the thickness of the extrusive layer.

5.1. Fracture Nucleation and Evolution

In this study, we have used the relationship between fractures and lava flows to make a distinction between fractures associated with fissure eruptions (group A) and fractures not associated with fissure eruptions (group B).

5.1.1. Group A: Deformation Associated With Dike Intrusions

The origin of the structure observed at the axis has been numerously discussed multiple times. For example, Haymon et al. (1991) propose that ASTs are the result of the drainback of elongated lava lakes into the eruptive fissure. The fissure walls would then form as a result of lava quenching when coming into contact with seawater during the fissure eruption. Other studies show that dike intrusions induce deformation directly above the dike (e.g., Carbotte et al., 2006; Lagabrielle & Cormier, 1999; Mastin & Pollard, 1988; Pollard et al., 1983; Soule et al., 2007). This type of deformation may result in the formation of a fissure or a graben with

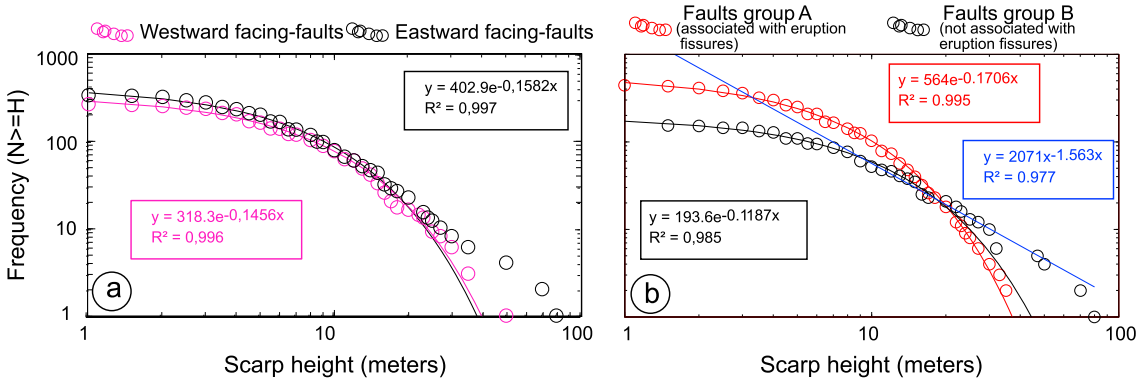

Figure 10. Cumulative frequency scarp height (H) log-log plots (*N* = number). (a) Cumulative frequency plot showing the differences between eastward (black) and westward facing (pink) faults. The exponential line fits are indicated. (b) Cumulative frequency plot showing the differences between "associated with eruption fissures" (group A in red) and "not associated with eruption fissures" (group B in black) faults. The respective exponential fits are shown in red and black, and the power line fit for the "nondike-induced" faults with scarp heights >10 m is shown in blue.

dimensions that are dependent on the width and depth of the dike (e.g., Mastin & Pollard, 1988; Pollard et al., 1983). In our study, even if some collapsed lava lakes are observed in the bottom of the ASTs, the presence of well-defined truncated pillow lavas (Figure 4a), lobate flows, or successive layers of sheet flows is not consistent with quenched lava, but instead suggest that they are the result of tectonic deformation occurring above the erupting dike. The width (<250 m) and depth (<10 m) of the relatively symmetrical grabens (Figure 3c), formed as a result of these fractures, are consistent with the dimensions of grabens formed by dike intrusions, with dikes widths inferior than 2 m and fault dips estimated to be 70–80° (e.g., Chadwick & Embley, 1998; Francheteau et al., 1990; Gudmundsson, 1995; Head et al., 1996; Kidd, 1977).

The presence of shallow dikes under the AST was confirmed by the study of Szitkar et al. (2016) on the 16°N segment, which is based on high-resolution near-seafloor magnetic data, and who observed magnetic anomalies, which they interpreted as dike swarms beneath each identified AST. Overlapping dike swarms are also identified where parallel ASTs are observed in the bathymetry, confirming the presence of a large active volcanic area. The formation of eruptive fissures on both sides of the ASTs indicates that this active volcanic zone reaches 1.8 km wide (Figure 6a). While only 15–20% of the EPR is characterized by ASTs wider than 500 m (and up to 2,000 m; Lagabrielle & Cormier, 1999), along the 16°N segment, this wide area of diking probably reflects the influence of equally wide magma lenses (up to 1,670 m in width) under the summit plateau (Carbotte et al., 2000). Therefore, the high density of fracture that we observe at the axis is probably induced by repeated dike intrusions, as it has been discovered along other fast spreading segments (e.g., Chadwick & Embley, 1998; Escartín et al., 2007; Fornari et al., 2004, 1998; Shah et al., 2003; Soule et al., 2007).

Along subsegments B and C, which are more densely fractured, the absence of recent lava flows associated with the graben (Figure 3c) does not necessarily indicated the absence of dike intrusions but may instead mean that the dike did not reach the surface in that location. Similar observations have been made at Axial Volcano during the eruption of 2011 and 2015 (Clague et al., 2017). Indeed, the analysis of near-bottom magnetic data collected simultaneously with the microbathymetric data (Szitkar et al., 2016) strongly suggests that dike swarms occur at shallow depth beneath the ridge axis. From our observations using microbathymetric data and dive videos, the absence of lava flows, posterior to the fractures, suggests that subsegments B and C are characterized by dike intrusions that produce few or no surface eruptions. Therefore, the deformation in these domains is better preserved, and successive dike intrusions without large volumes of lava flow may have increased the graben depth and width by a focusing of the stress into preexisting fractures. Using those observation, the along axis variation of the fracture density in group A probably reflects variations in the ability of dikes to reach the surface and to produce eruptions, as previously suggested by Le Saout et al. (2014).

5.1.2. Group B: Deformation Not Affected by Dike

Just outside of the AST, traces of fractures are frequently found to be covered by lava flows (Figure 6a), which explains the fast decrease in observable fractures near the ridge axis. Although this region is not affected by dike intrusions, it is not completely devoid of fractures as shown in Figure 6. These fractures consist of fissures and faults, in similar proportions to those induced by dike intrusions (~15% of fissures and 85% of faults). In this off-axis region, faults do not always form grabens, but when they do, the graben formed is generally asymmetric and they are different to the geometry of the fractures induced by dike intrusions. Various hypotheses may explain the presence of fractures in the off-axis region. First, some of these fractures may have been nucleated along the axis and were preserved. Indeed, some regions have low repaving rates due to (1) variations in the eruptive activity, with periods associated of low magma supply and eruption (for example, subsegments B and C; Figure 6); Cormier et al., 2003; Fornari et al., 1998), or (2) the presence of inward facing faults that served as dams to the more recent volcanic activity (for example, the western flank of subsegment D; Figure 7). However, this hypothesis does not explain all the fractures observed in the off-axis region. Some fissures and small faults formed after the lava flows emplacement, which suggests that fractures also nucleate away from the active volcanic zone or, at least, were reactivated in response to other constraints. Indeed, Escartín et al. (2007) proposed that the development of fractures associated with dike intrusion is decoupled from the development of off-axis fracture.

5.1.3. Comparison Between Fractures From Groups A and B

Comparisons between fractures from groups A and B also show variations in the deformation regimes. The cumulative size-frequency distribution of fault scarps induced by dike intrusions (group A) follows an

exponential distribution (Figure 10b), suggesting that on axis fractures in the studied area could be in either a nucleation regime, a coalescence regime, or a saturation regime (e.g., Ackermann et al., 2001; Ackermann & Schlische, 1997; Bonnet et al., 2001; Carbotte & Macdonald, 1994b; Cowie et al., 1993, 1995; Deschamps et al., 2007). The low throw/length ratio of ~0.0067 of these on-axis fractures (Figure 8e) is generally associated with elongation rather than vertical growth of the fractures. Moreover, the variable spacing of the fractures suggests that the fractures from group A did not reach a saturation regime, which would result in proportionally spaced fractures. Therefore, fractures from group A are rather in a nucleation regime or a coalescence regime that traduce the appearance of new fractures or the lengthening by linkage to preexisting fractures (e.g., Deschamps et al., 2007). Off-axis fractures (group B) are mainly characterized by a higher throw/length ratio of 0.0202, which can be associated with a vertical growth of the fault scarps. We also observe a cumulative size-frequency distribution of off-axis fault scarps that tends to follow a power law distribution, for fault with vertical throw higher than 10 m. This observation indicates that on the edge of the plateau, fractures are in a "growth regime" stage, with an increase of the vertical throw. Differences in the deformation regimes may result from an underestimation of fracture geometry due to partial erasure by younger lava flows, but they may also indicate changes in deformation constraints that form and affect these structures as they move away from the ridge axis. This second hypothesis is confirmed by observations along the EPR, which shows that the normal faulting initiates between 600 m and 4 km away from the ridge axis (e.g., Fornari et al., 1998; Garel et al., 2002; Macdonald, 1982; Searle, 1984; Wright, Haymon, & Fornari, 1995; Wright, Haymon, & MacDonald, 1995). Along the 16°N segment, the initiation of off-axis fractures occurs as close as 755 m from the ridge axis (Figure 7).

5.2. Relation Between Deformation and Internal Lithospheric Structure

In this section, we will focus on the subsegment D, where the presence of two overlapping ASTs, with the eastern AST being more volcanically active, results in an asymmetry in the lava flow distribution between the eastern and western parts of the plateau (Figures 6a and 7). On the western part of the summit plateau, lave flows tend to be confined within the western AST, allowing us to (1) observe the deformation pattern that is not overprinted by recent lava flows and (2) analyze the distribution of the brittle extension in this region.

Escartín et al. (2007) suggests that location of the initiation of the brittle deformation reflects the variations in the lithosphere, which thickens and cools rapidly away from the ridge axis due to strong hydrothermal activity at the edge of the AML (e.g., Dunn et al., 2000; Maclennan et al., 2005; Singh et al., 1999). A thin, weak, and hot lithosphere above an AML inhibits the nucleation of fractures resulting from the brittle extension (e.g., Carbotte et al., 1997; Carbotte & Macdonald, 1994b; Fornari et al., 1998). At 16°N, the ridge axis interacts with the Mathematician hot spot resulting in a wide region of high temperatures and crustal melting, as suggested the shape of the ridge, the bull's-eye gravity anomalies (Shah & Buck, 2006), and the presence of an off-axis magma lens beneath the western part of the summit plateau (Figures 6d and 11; Carbotte et al., 2000). Hydrothermal activity is also particularly low along the ridge (Baker et al., 2001), which promotes the conservation of the heat in the lithosphere. This suggests that at a similar distance from the ridge axis, the 16°N segment lithosphere is probably warmer and thinner than for other ridges that are not affected by a hot spot (Shah & Buck, 2006). Therefore, along the 16°N segment, the brittle deformation would be expected to occur further away from the ridge axis compared to other EPR segments that does not interact with a hot spot. However, we observe that the distance from the ridge axis to observable first evidence of the brittle extension is consistent with studies along other fast spreading ridges without hot spot (or equivalent) activity, which is suggested to be between 600 and 4 km from the ridge axis (e.g., Fornari et al., 1998; Garel et al., 2002; Macdonald, 1982; Searle, 1984; Wright, Haymon, & Fornari, 1995; Wright, Haymon, & MacDonald, 1995). Therefore, the proximity of the Mathematician hot spot seems to have no significant impact on the initiation of the brittle extension at 16°N.

Comparing the distribution of fractures to the geometry of layer 2A (Figure 6d), we note that fractures linked to dike intrusions (group A) are focused on the thin part of the layer 2A. Beyond this thin region, the thickness of layer 2A increases rapidly from 100 to 300 m between, at distances 350 and 750 m from the ridge axis (Carbotte et al., 2000). This observation is consistent with the theory that the thickening of layer 2A mainly occurs through diking and associated eruptions at the axis, within in a relatively narrow area (e.g., Carbotte, 2001; Harding et al., 1993; Vera & Diebold, 1994).

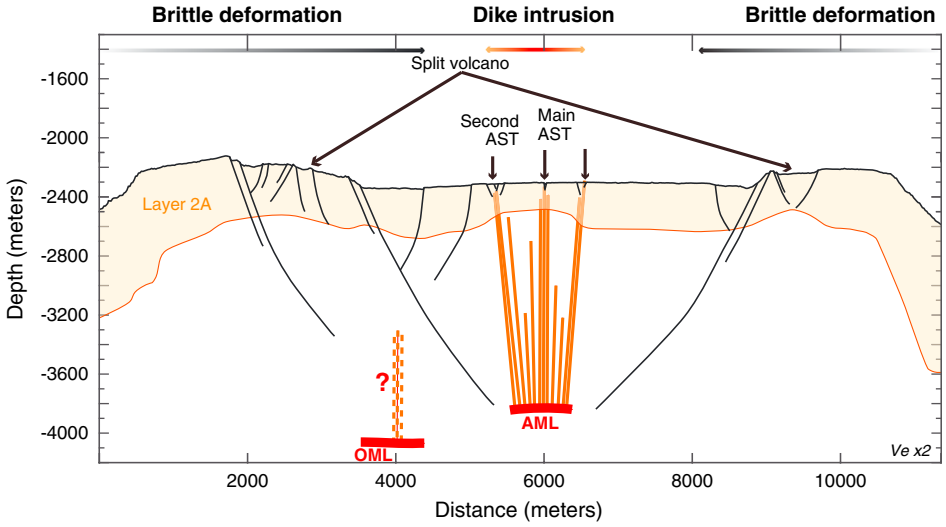

Figure 11. Profile perpendicular to the third-order spreading subsegment D intersecting the axis at 15°42′N (a green line marks the location of this profile in Figure 6), showing the deep structure of this segment and its relationship with the seafloor fractures with a vertical exaggeration is of 2. The layer 2A (baseline in orange) and the depth and lateral extension of the axial magma lens (AML) and off-axis magma lens (OML) are based on the across-axis seismic reflection profile 1341 from Carbotte et al. (2000). Dikes are shown by vertical orange lines (solid for AML and dashed for OML) and fractures by black lines with a dip of 60°. The different domains of deformation are indicated at the top of the figure.

Outside the thin layer 2A region, fractures are probably not induced by dike intrusions, but instead are more likely to result from extension, which is either induced by changes in the AML or by the regional stress (ref). Mechanical approaches show that brittle extension beyond the AML can result in regional extension and/or withdrawal of the magma lens (e.g., Garel et al., 2002). In the case where the brittle extension is linked to magma lens withdrawal, mechanical models suggest that the initial (closest to the axis) inward facing faults that formed without any dike intrusions will be linked to the edges of the AML (Garel et al., 2002). Therefore, the distance from the ridge axis of these first inward facing faults will depend on the width and depth of the AML. The narrower the AML, the closer to the axis these first fractures will be. In subsegment D (Figures 6 and 7), considering the width (750–800 m) and the depth of the AML below the seafloor (1,400-1,500 m), and assuming a mean normal fault dip of 60°, we estimate that the first inward facing faults induced by deflation of the AML will be located between 1,180 and 1,270 m from the ridge axis. From our observation of subsegment D, the first inward facing faults are located beyond this calculated 1,180–1,270 m region, at ~2,000 m from the ridge axis (Figure 11). This difference between the calculated and observed distances may reflect the absence of significant changes in the dimensions of the AML in the recent period, or it may indicate that the deformation induced by changes in the AML is sustained by these outer faults until the distance between the edges of the AML and the faults reaches a threshold point. Prior to that inward facing faults, all fractures associated with the brittle deformation corresponds to outward facing faults or fissures. If we consider these outward facing faults to be conjugate fractures from the inward facing faults, their locations at 750 m from the axis (Figure 7) are thus consistent with deformation induced by volume changes at the edge of the AML.

If the AML have a direct impact on the deformation induced by the magmatic intrusions and AML volume changes, there is no direct observable evidence of significant deformation resulting from the off-axis magma lens on the western half of the plateau. Indeed, directly above the off-axis magma lens, we do not observe any evidence of eruptive fissures with surrounding lava flows or the formation of symmetrical grabens (as observed above the AML). Therefore, the absence of significant variations in thickness of the layer 2A and its relative symmetry with respect to the main ridge axis suggest that magmatic eruptions occur at the axis, which resulted in the thickening of the layer 2A on the summit plateau. In subsegment B, fractures induced by brittle extension are also observed in the eastern half of the plateau, regardless of the presence of the off-axis magma lens. This suggests that the off-axis magma lens has no direct influence on the deformation or that the influence is not significant enough to be distinct from the main deformation regime. The nil or small effect of the off-axis magma lens cannot be related to the depth of this magma lens (~1,700 m beneath the

seafloor), as deeper AMLs are known to be the source of eruptions, for example, along the Galapagos Spreading Center where AMLs are located at 1.7–2.5 km beneath the seafloor (Chen & Lin, 2004). In the 16°N EPR studied area, the absence of significant deformation directly above the off-axis magma lens may suggest that the magmatic activity associated with this off-axis lens during at least the last 3 kyr (i.e., the maximum age of the lava flows above the magma lens; Carlut et al., 2004) is either really low and/or is not directly connected to the plateau.

5.3. Tectonic Strain Estimation

To estimate the bias due to both volcanic processes and assumptions regarding fault geometries, we now assess the tectonic strain in subsegments C and D: (1) in subsegment C, where fractures induced by dike intrusion are less overprinted by lava flow or where more deformation occurs, and (2) in subsegment D where fault overprinting seems more important at the axis and brittle extension occurs beyond the AML. The tectonic strain is calculated along five cross-axis profiles located between 15°41′N and 15°46′N (Figure 2c) using equations (1) and (2):

$$D = T \times \frac{1}{\tan\alpha} \tag{1}$$

where D is the cumulative horizontal displacement along each profile, T is the cumulative throw, and α is the mean dip of the fault dip. The tectonic strain (Ts) along each profile is given by equation (2):

$$Ts = 100 \times \frac{D}{L} \tag{2}$$

where L is the length of the profile (4,800 m).

Taking into account that our survey revealed an underestimation of the fracture dip due to coverage with lava flow talus slope on the scarps, we calculate fault strains using dips ranging from 60° to 80° that characterize the original fault dips (e.g., Deschamps et al., 2007) and also correspond to the most common dip values measured (Figure 8d). This choice is supported by submersible observations (this study and Mitchell et al., 2000) and is also consistent with fault dips measured along the Explorer ridge (Deschamps et al., 2007) and along the 9°N EPR segment (Escartín et al., 2007). The calculated strain ranges from 0.1 to 0.7% for a dip of 80°, 1 to 4.9% for a dip of 70°, and 3.8 to 19% assuming an average dip of 60° (Figure 12a). These dip values represent the contribution of tectonic structures to plate divergence within a 4,800-m-wide zone across the ridge axis. The maximum age of the lava flows on the plateau is 2–3 ka (Carlut et al., 2004) and postdates the formation of the fractures. Considering this timer period and a profile length of 4,800 m, the approximate extension rate associated with a dip of 80° varies from 1.6 to 17 mm/year, 64 to 117 mm/year for a dip of 70°, and 60 to 456 mm/year assuming an average dip of 60°. As the spreading rate of the 16°N segment is 85 mm/year (Weiland & Macdonald, 1996) an average dip of 70° for the fractures is the most probable. In addition, this 70° dip tectonic strain of 1–4.9% is similar to the 1–3% strain measured between 9.4°N and 10°N on the EPR assuming fault dip of 45° (Escartín et al., 2007). The EPR shows evidence of relatively low tectonic strain compared to a measurement along the intermediate Explorer Ridge (3.7–18.4% assuming fault dips of 60–80°; Deschamps et al., 2007), which is consistent with divergence along fast spreading ridges primarily accommodated by volcanism and a smaller proportion by fractures. However, the tectonic strain may be highly underestimated due to volcanic overprinting that partially or fully buries some faults (e.g., Alexander & Macdonald, 1996; Bohnenstiehl & Kleinrock, 2000; Carbotte et al., 1997). Indeed, a larger tectonic strain of 5% is observed in the subsegment C (Figure 12b) where faults are less overprinted by lava flows.

Figure 12 shows that the tectonic strain remains relatively constant along subsegment D. This indicates that the deformation and/or the amount of overprinting of fractures by lava flows is constant within this subsegment. In contrast, we observe a big difference between subsegments C and D, with the tectonic strain rate in subsegment D being much higher than in subsegment C—an average of 5% versus 1.45% using a dip value of 70°, and 19% versus 5.5% with a dip of 80°, for subsegments C and D, respectively. Assuming that variation between subsegments C and D is only due to the volume of lava flow erupted and thus proportion of the fractures overprinted, we estimate that this difference indicates that at least 70% of the fractures are buried by lava flows in the subsegment D. This estimate is very similar to the 75% overprinting value estimated by Escartín et al. (2007) for the 9°N segment.

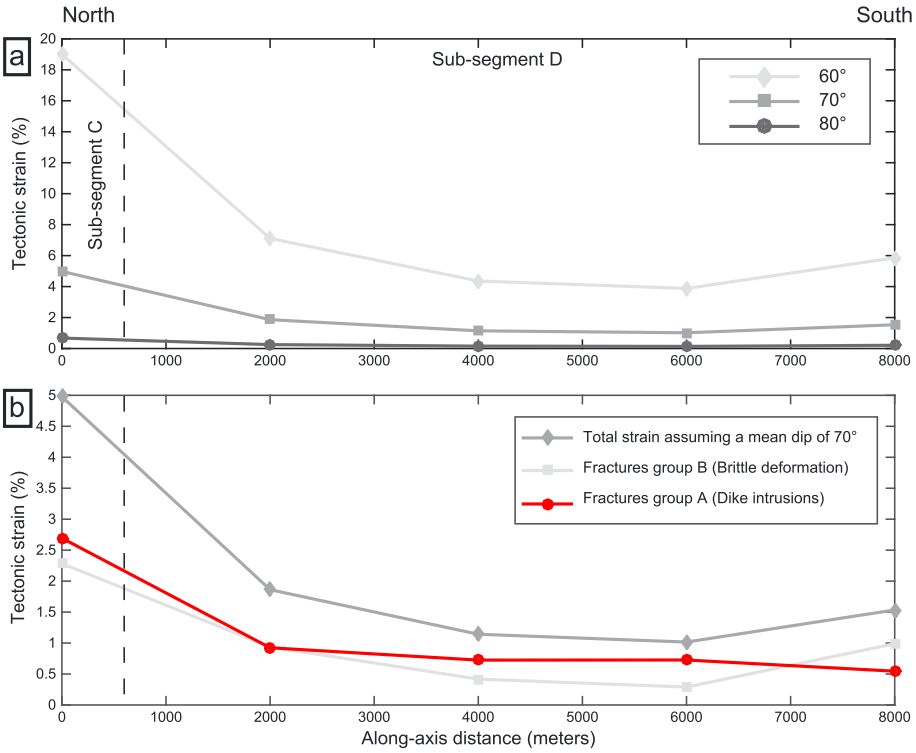

Figure 12. Evaluation of tectonic strain along subsegments C and D using five across-axis 4,800 m-long profiles (profile locations are marked in Figure 2c). The vertical dashed line indicates the boundary between subsegments C and D. (a) Contribution of extension along fault scarps, computed using mean fault dips of 60°, 70°, and 80°. (b) Total tectonic strain calculated using a mean fault dip of 70° (dark grey diamonds), strain accommodated by fractures induced by dike intrusions (red circles), and from brittle extension (light grey squares).

In subsegment D, on the western part of the plateau, the western AST is characterized by a low volcanic activity and acts as a barrier to lava flows erupting from the eastern AST (Figure 7). Therefore, fractures induced by brittle extension on the western plateau are protected from overprinting by lava flows. Our observations show that these fractures (i.e., "group B") are not affected or related to recent volcanic activity. As a consequence, we assume that these fractures are located within a relatively older seafloor, compared to the fractures that are associated with dike intrusions (i.e., "group A"). This group A/B versus age distinction is similar to the "young"/"old" seafloor distinction proposed by Escartín et al. (2007) for 9°N segment. Escartín et al. (2007) observed that even knowing the underestimation of fractures due to lava flow overprinting, the tectonic strain is lower for young seafloor ($<$1%) compared to older seafloor ($>$2%). In our present study, and regardless of the levels of volcanic activity along the ASTs, the tectonic strain rate is very similar or slightly higher in younger seafloor (0.5–27% for fractures induced by dike intrusion) compared to older seafloor (0.2–2.3% for fractures affected by brittle deformation). Higher tectonic strain in younger seafloor suggests that (1) the deformation induced by dike intrusions is more important and/or is better preserved by low lava flow overprinting levels at the ridge axis, due to fewer eruptions or smaller volumes; (2) the "older" seafloor is affected by more lava flow overprinting; and/or (3) the degree of brittle deformation in the 16°N segment is lower than in the 9°N EPR segment. However, this lower apparent brittle deformation rate is consistent with the higher magma budget and thermal state of the ridge related to the locality of the Mathematician hot spot.

6. Conclusion

The joint analysis of high-resolution bathymetric data and submersible dive photographs and videos documents tectonic patterns and their relationship with lava flows, within the central part of the 16°N segment of the EPR. These data allow us to quantify the deformation in this area and to relate sea-bottom deformation to the deep structure of the ridge (i.e., AML and layer 2A). Our study supports the following conclusions:

1. Along the 16°N segment, more than 70% of the fractures are associated with eruptions as shown by the direction of lava flows and the location of lava channels. The fracture geometry and near-seafloor magnetism (Szitkar et al., 2016) indicate that they correspond to fractures located at the source of lava flows, probably induced by one or more dike intrusions. The distribution of these dike-induced fractures implies an active volcanic area that is 1.8 km wide, which is consistent with a wide AML underlying the ridge axis.
2. The vertical throw cumulative frequency plot (Figure 10b) suggests that fractures located near and within the ASTs that were induced by dike intrusions nucleated recently and/or evolved mainly due to linkage of existing fractures. In contrast, away from the ridge axis, fractures that evolved or nucleated via brittle extension mainly grow by an increase of their vertical throw rather than by linkage with existing fractures.
3. The first evidence of brittle extension is found 755 m from the ridge axis, a distance similar to those observed in other parts of the EPR (e.g., Carbotte et al., 1997; Garel et al., 2002). Thus, the high magmatic budget and temperature of the ridge axis, induced by the proximity of the Mathematician hot spot, have no significant impact on the location of the brittle extension. This brittle extension affects fractures that nucleate and evolve on a seafloor that is underlain by a relatively thick layer 2A (>350 m) that are induced by AML volume changes or by the regional extensional. The off-axis magma lens appears to have no significant direct influence on the geometry of the layer 2A nor on the location of the brittle extension.
4. For subsegments C and D, faults accommodate 0.1–19% of the width of the summit plateau, assuming fault dips ranging from 60° to 80°. The amount of deformation accommodated by fractures appears more important in subsegment C (5%) compared to subsegment D (1.45%). Our study reveals that this difference mainly reflects the effect of the overprinting of the tectonic structures in subsegment D by lava flows, where at least 70% of the fractures are covered by magmatic flows, and therefore, the tectonic strain is highly underestimated.
5. The tectonic strain along the summit of the 16°N is similar to the strain rates calculated at 9°N on the EPR (Escartín et al., 2007). However, Escartín et al. (2007) show that the tectonic strain is lower in the young seafloor, whereas in the 16°N segment, the tectonic strain is similar or slightly higher for fractures induced by dike intrusion (group A) compared to those induced by brittle deformation (group B). Assuming that the group A fractures are mostly located in the younger seafloor, this difference suggests that for the 16°N segment, the deformation induced by dikes is more important or better preserved, and/or the amount of brittle deformation is lower. Combined with the small number of fractures that have evolved from through brittle extension, our study reveals that the Mathematician hot spot, located on this spreading axis, may result in the formation of less brittle extension fractures.

Acknowledgments
We thank the crew of the R/V l'Atalante, the engineers, and technicians from Genavir and the scientific teams of PARISUB. This work was supported by a PhD Scholarship of Region Bretagne and Université de Bretagne Occidentale (France) and has benefited from funding by the Labex-Mer of the "Institut Universitaire Européen de la Mer" (IUEM) and Europôle Mer. The data are available through the NAUTILUS portal (http://campagnes.flotteoceanographique.fr/ campagnes/10010020/). This paper is dedicated to the memory of Anne Deschamps, who was involved in this project from the acquisition to the interpretation of the high-resolution bathymetry, photographs, and videos.

References

Ackermann, R. V., & Schlische, R. W. (1997). Anticlustering of small normal faults around larger faults. *Geology*, *25*(12), 1127–1130. https://doi.org/10.1130/0091-7613(1997)025<1127:AOSNFA>2.3.CO;2

Ackermann, R. V., Schlische, R. W., & Withjack, M. O. (2001). The geometric and statistical evolution of normal fault systems: An experimental study of the effects of mechanical layer thickness on scaling laws. *Journal of Structural Geology*, *23*(11), 1803–1819. https://doi.org/10.1016/S0191-8141(01)00028-1

Alexander, R. T., & Macdonald, K. C. (1996). Sea Beam, SeaMARC II and ALVIN-based studies of faulting on the East Pacific Rise 9°20′N–9°50′N. *Marine Geophysical Researches*, *18*(5), 557–587. https://doi.org/10.1007/BF00310069

Baker, E. T., Cormier, M.-H., Langmuir, C. H., & Zavala, K. (2001). Hydrothermal plumes along segments of contrasting magmatic influence, 15°20′–18°30′N, East Pacific Rise: Influence of axial faulting. *Geochemistry, Geophysics, Geosystems*, *2*(9), 1051. https://doi.org/10.1029/2000GC000165

Bohnenstiehl, D. R., & Carbotte, S. M. (2001). Faulting patterns near 19°30′S on the East Pacific Rise: Fault formation and growth at a superfast spreading center. *Geochemistry, Geophysics, Geosystems*, *2*(9), 1056. https://doi.org/10.1029/2001GC000156

Bohnenstiehl, D. R., & Kleinrock, M. C. (1999). Faulting and fault scaling on the median valley floor of the trans-Atlantic geotraverse (TAG) segment, 26°N on the Mid-Atlantic Ridge. *Journal of Geophysical Research*, *104*(B12), 29,351–29,364. https://doi.org/10.1029/1999JB900256

Bohnenstiehl, D. R., & Kleinrock, M. C. (2000). Fissuring near the TAG active hydrothermal mound, 26 N on the Mid-Atlantic Ridge. *Journal of Volcanology and Geothermal Research*, *98*(1-4), 33–48. https://doi.org/10.1016/S0377-0273(99)00192-4

Bonnet, E., Bour, O., Odling, N. E., Davy, P., Main, I., Cowie, P., & Berkowitz, B. (2001). Scaling of fracture systems in geological media. *Reviews of Geophysics*, *39*(3), 347–383. https://doi.org/10.1029/1999RG000074

Canales, J. P., Ito, G., Detrick, R. S., & Sinton, J. (2002). Crustal thickness along the western Galápagos Spreading Center and the compensation of the Galápagos hotspot swell. *Earth and Planetary Science Letters*, *203*(1), 311–327. https://doi.org/10.1016/S0012-821X(02)00843-9

Carbotte, S. M. (2001). Mid-ocean ridge seismic structure. In J. H. Steele, S. A. Thorpe, & K. K. Turekian (Eds.), *Encyclopedia of Ocean Sciences* 1st Edition (pp. 1220–1228). London: Academic.

Carbotte, S. M., Detrick, R. S., Harding, A., Canales, J. P., Babcock, J., Kent, G., et al. (2006). Rift topography linked to magmatism at the intermediate spreading Juan de Fuca Ridge. *Geology*, *34*(3), 209–212. https://doi.org/10.1130/G21969.1

Carbotte, S. M., & Macdonald, K. C. (1994a). The axial topographic high at intermediate and fast spreading ridges. *Earth and Planetary Science Letters*, *128*(3-4), 85–97. https://doi.org/10.1016/0012-821X(94)90137-6.

Carbotte, S. M., & Macdonald, K. C. (1994b). Comparison of seafloor tectonic fabric at intermediate, fast, and super fast spreading ridges: Influence of spreading rate, plate motions, and ridge segmentation on fault patterns. *Journal of Geophysical Research*, *99*(B7), 13,609–13,631. https://doi.org/10.1029/93JB02971

Carbotte, S. M., Mutter, C., Mutter, J. C., & Ponce-Correa, G. (1998). Influence of magma supply and spreading rate on crustal magma bodies and emplacement of the extrusive layer; insights from the East Pacific Rise at lat 16°N. *Geology*, *26*(5), 455–458. https://doi.org/10.1130/0091-7613(1998)026<0455:IOMSAS>2.3.CO;2

Carbotte, S. M., Mutter, J. C., & Xu, L. (1997). Contribution of volcanism and tectonism to axial and flank morphology of the southern East Pacific Rise, 17°10′-17°40′S, from a study of layer 2A geometry. *Journal of Geophysical Research*, *102*(B5), 10,165–10,184. https://doi.org/10.1029/96JB03910

Carbotte, S. M., Ryan, W. B. F., Jin, W., Cormier, M.-H., Bergmanis, E., Sinton, J., & White, S. (2003). Magmatic subsidence of the East Pacific Rise (EPR) at 18°14′S revealed through fault restoration of ridge crest bathymetry. *Geochemistry, Geophysics, Geosystems*, *4*(1), 1008. https://doi.org/10.1029/2002GC000337

Carbotte, S. M., Solomon, A., & Ponce-Correa, G. (2000). Evaluation of morphological indicators of magma supply and segmentation from a seismic reflection study of the East Pacific Rise 15°30′–17°N. *Journal of Geophysical Research*, *105*(B2), 2737–2759. https://doi.org/10.1029/1999JB900245

Carlut, J., Cormier, M.-H., Kent, D. V., Donnelly, K. E., & Langmuir, C. H. (2004). Timing of volcanism along the northern East Pacific Rise based on paleointensity experiments on basaltic glasses. *Journal of Geophysical Research*, *109*, B04104. http://doi.org/10.1029/2003JB002672

Chadwick, W. W., Clague, D. A., Embley, R. W., Perfit, M. R., Butterfield, D. A., Caress, D. W., et al. (2013). The 1998 eruption of Axial Seamount: New insights on submarine lava flow emplacement from high-resolution mapping. *Geochemistry, Geophysics, Geosystems*, *14*, 3939–3968. https://doi.org/10.1002/ggge.20202

Chadwick, W. W., & Embley, R. W. (1998). Graben formation associated with recent dike intrusions and volcanic eruptions on the mid-ocean ridge. *Journal of Geophysical Research*, *103*(B5), 9807–9825. https://doi.org/10.1029/97JB02485

Chen, Y. J., & Lin, J. (2004). High sensitivity of ocean ridge thermal structure to changes in magma supply: The Galapagos Spreading Center. *Earth and Planetary Science Letters*, *221*(1-4), 263–273. https://doi.org/10.1016/S0012-821X(04)00099-8

Christie, D. M., Werner, R., Hauff, F., Hoernle, K., & Hanan, B. B. (2005). Morphological and geochemical variations along the eastern Galápagos Spreading Center. *Geochemistry, Geophysics, Geosystems*, *6*, Q01006. https://doi.org/10.1029/2004GC000714

Clague, D., Dreyer, B. M., Paduan, J. B., Martin, J. F., Caress, D. W., Gill, J. B., et al. (2014). Eruptive and tectonic history of the Endeavour Segment, Juan de Fuca Ridge, based on AUV mapping data and lava flow ages. *Geochemistry, Geophysics, Geosystems*, *15*, 3364–3391. https://doi.org/10.1002/2014GC005415

Clague, D. A., Paduan, J. B., Caress, D. W., Chadwick, W. W. Jr., Le Saout, M., Dreyer, B. M., & Portner, R. A. (2017). High-resolution AUV mapping and targeted ROV observations of three historical lava flows at Axial Seamount. *Oceanography*, *30*(4), 82–99. https://doi.org/10.5670/oceano.2017.426

Cormier, M.-H., Ryan, W. B. F., Shah, A. K., Jin, W., Bradley, A. M., & Yoerger, D. R. (2003). Waxing and waning volcanism along the East Pacific Rise on a millennium time scale. *Geology*, *31*(7), 633–636. https://doi.org/10.1130/0091-7613(2003)031<0633:WAWVAT>2.0.CO;2

Cowie, P. A. (1998). Normal fault growth in three-dimensions in continental and oceanic crust. In W. R. Buck, P. T. Delaney, J. A. Karson, & Y. Lagabrielle (Eds.), *Faulting and Magmatism at Mid-Ocean Ridges, Geophysical Monograph Series* (Vol. 106, pp. 325–348). Washington, DC: American Geophysical Union. https://doi.org/10.1029/GM106p0325

Cowie, P. A., Sornette, D., & Vanneste, C. (1995). Multifractal scaling properties of a growing fault population. *Geophysical Journal International*, *122*(2), 457–469. https://doi.org/10.1111/j.1365-246X.1995.tb07007.x

Cowie, P. A., Vanneste, C., & Sornette, D. (1993). Statistical physics model for the spatiotemporal evolution of faults. *Journal of Geophysical Research*, *98*(B12), 21,809–21,821. https://doi.org/10.1029/93JB02223

Crowder, L. K., & Macdonald, K. C. (2000). New constraints on the width of the zone of active faulting on the East Pacific Rise 8° 30′N–10° 00′N from Sea Beam Bathymetry and SeaMARC II Side-scan Sonar. *Marine Geophysical Researches*, *21*(6), 513–527. https://doi.org/10.1023/A:1004875609890

Deschamps, A., Grigné, C., Le Saout, M., Soule, S. A., Allemand, P., Vliet-Lanoe, V., et al. (2014). Morphology and dynamics of inflated subaqueous basaltic lava flows. *Geochemistry, Geophysics, Geosystems*, *15*, 2128–2150. https://doi.org/10.1002/2014GC005274

Deschamps, A., Tivey, M., Embley, R. W., & Chadwick, W. W. (2007). Quantitative study of the deformation at Southern Explorer Ridge using high-resolution bathymetric data. *Earth and Planetary Science Letters*, *259*(1–17), 1–2. https://doi.org/10.1016/j.epsl.2007.04.007

Detrick, R. S., Sinton, J. M., Ito, G., Canales, J. P., Behn, M., Blacic, T., et al. (2002). Correlated geophysical, geochemical, and volcanological manifestations of plume-ridge interaction along the Galápagos Spreading Center. *Geochemistry, Geophysics, Geosystems*, *3*(10), 8501. https://doi.org/10.1029/2002GC000350

Dunn, R. A., Toomey, D. R., & Solomon, S. C. (2000). Three-dimensional seismic structure and physical properties of the crust and shallow mantle beneath the East Pacific Rise at 9° 30′N. *Journal of Geophysical Research*, *105*(B10), 23,537–23,555. https://doi.org/10.1029/2000JB900210

Embley, R. W., & Chadwick, W. W. (1994). Volcanic and hydrothermal processes associated with a recent phase of seafloor spreading at the northern Cleft segment: Juan de Fuca Ridge. *Journal of Geophysical Research*, *99*(B3), 4741–4760. https://doi.org/10.1029/93JB02038

Escartín, J., Soule, S. A., Fornari, D. J., Tivey, M. A., Schouten, H., & Perfit, M. R. (2007). Interplay between faults and lava flows in construction of the upper oceanic crust: The East Pacific Rise crest 9°25′–9°58′N. *Geochemistry, Geophysics, Geosystems*, *8*, Q06005. https://doi.org/10.1029/2006GC001399

Ferrini, V. L., Fornari, D. J., Shank, T. M., Kinsey, J. C., Tivey, M. A., Soule, S. A., et al. (2007). Submeter bathymetric mapping of volcanic and hydrothermal features on the East Pacific Rise crest at 9°50′N. *Geochemistry, Geophysics, Geosystems*, *8*, Q01006. https://doi.org/10.1029/2006GC001333

Fink, J. H., & Fletcher, R. C. (1978). Ropy pahoehoe: Surface folding of a viscous fluid. *Journal of Volcanology and Geothermal Research*, *4*(1-2), 151–170. https://doi.org/10.1016/0377-0273(78)90034-3

Fink, J. H., & Griffiths, R. W. (1998). Morphology, eruption rates, and rheology of lava domes: Insights from laboratory models. *Journal of Geophysical Research*, *103*(B1), 527–545. https://doi.org/10.1029/97JB02838

Fornari, D., Tivey, M., Schouten, H., Perfit, M., Yoerger, D., Bradley, A., et al. (2004). Submarine lava flow emplacement at the East Pacific Rise 9°50′N: Implications for Uppermost Ocean crust stratigraphy and hydrothermal fluid circulation. In C. R. German, J. Lin, & L. M. Parson (Eds.), *Mid-ocean ridges: Hydrothermal interactions between the lithosphere and oceans, Geophysical Monograph Series* (Vol. 148, pp. 187–218). Washington, DC: American Geophysical Union. https://doi.org/10.1029/148GM08

Fornari, D. J., Haymon, R. M., Perfit, M. R., Gregg, T. K. P., & Edwards, M. H. (1998). Axial summit trough of the East Pacific Rise 9°−10°N: Geological characteristics and evolution of the axial zone on fast spreading mid-ocean ridges. *Journal of Geophysical Research*, *103*(B5), 9827–9855. https://doi.org/10.1029/98JB00028

Francheteau, J., Armijo, R., Cheminée, J. L., Hekinian, R., Lonsdale, P., & Blum, N. (1990). 1 Ma East Pacific Rise oceanic crust and uppermost mantle exposed by rifting in Hess Deep (equatorial Pacific Ocean). *Earth and Planetary Science Letters*, *101*(2-4), 281–295. https://doi.org/10.1016/0012-821X(90)90160-Y

Garel, E., Dauteuil, O., & Lagabrielle, Y. (2002). Deformation processes at fast to ultra-fast oceanic spreading axes; mechanical approach. *Tectonophysics*, *346*(3-4), 223–246. https://doi.org/10.1016/S0040-1951(01)00280-3

Gregg, T. K., & Smith, D. K. (2003). Volcanic investigations of the Puna Ridge, Hawai'i: Relations of lava flow morphologies and underlying slopes. *Journal of Volcanology and Geothermal Research*, *126*(1-2), 63–77. https://doi.org/10.1016/S0377-0273(03)00116-1

Gregg, T. K. P., & Fink, J. H. (1995). Quantification of submarine lava-flow morphology through analog experiments. *Geology*, *23*(1), 73–76. https://doi.org/10.1130/0091-7613(1995)023<0073:QOSLFM>2.3.CO;2

Gudmundsson, A. (1995). Infrastructure and mechanics of volcanic systems in Iceland. *Journal of Volcanology and Geothermal Research*, *64*(1–2), 1–22. https://doi.org/10.1016/0377-0273(95)92782-Q

Harding, A. J., Kent, G. M., & Orcutt, J. (1993). A multichannel seismic investigation of upper crustal structure at 9 N on the East Pacific Rise: Implications for crustal accretion. *Journal of Geophysical Research*, *98*(B8), 13,925–13,944. https://doi.org/10.1029/93JB00886

Haymon, R. M., Fornari, D. J., Edwards, M. H., Carbotte, S. M., Wright, D., & MacDonald, K. C. (1991). Hydrothermal vent distribution along the East Pacific Rise crest (9°09′–54′N) and its relationship to magmatic and tectonic processes on fast-spreading mid-ocean ridges. *Earth and Planetary Science Letters*, *104*(2–4), 513–534. https://doi.org/10.1016/0012-821X(91)90226-8

Head, J. W., Wilson, L., & Smith, D. K. (1996). Mid-ocean ridge eruptive vent morphology and substructure: Evidence for dike widths, eruption rates, and evolution of eruptions and axial volcanic ridges. *Journal of Geophysical Research*, *101*(B12), 28,265–28,280. https://doi.org/10.1029/96JB02275

Hooft, E. E., Schouten, H., & Detrick, R. S. (1996). Constraining crustal emplacement processes from the variation in seismic layer 2A thickness at the East Pacific Rise. *Earth and Planetary Science Letters*, *18*(8), 2906–2929. https://doi.org/10.1002/2017GC006980

Ingle, S., Ito, G., Mahoney, J. J., Chazey, W., Sinton, J., Rotella, M., & Christie, D. M. (2010). Mechanisms of geochemical and geophysical variations along the western Galápagos Spreading Center. *Geochemistry, Geophysics, Geosystems*, *11*, Q04003. https://doi.org/10.1029/2009GC002694

Kidd, R. G. W. (1977). A model for the process of formation of the upper oceanic crust. *Geophysical Journal International*, *50*(1), 149–183. https://doi.org/10.1111/j.1365-246X.1977.tb01328.x

Lagabrielle, Y., & Cormier, M.-H. (1999). Formation of large summit troughs along the East Pacific Rise as collapse calderas: An evolutionary model. *Journal of Geophysical Research*, *104*(B6), 12,971–12,988. https://doi.org/10.1029/1999JB900015

Lagabrielle, Y., Garel, E., Dauteuil, O., & Cormier, M.-H. (2001). Extensional faulting and caldera collapse in the axial region of fast spreading ridges; analog modeling. *Journal of Geophysical Research*, *106*(B2), 2005–2015. https://doi.org/10.1029/2000JB900266

Le Saout, M., Deschamps, A., Soule, S. A., & Gente, P. (2014). Segmentation and eruptive activity along the East Pacific Rise at 16 N, in relation with the nearby Mathematician hotspot. *Geochemistry, Geophysics, Geosystems*, *15*, 4380–4399. https://doi.org/10.1002/2014GC005560

Macdonald, K. C. (1982). Mid-ocean ridges: Fine scale tectonic, volcanic and hydrothermal processes within the plate boundary zone. *Annual Review of Earth and Planetary Sciences*, *10*(1), 155–190. https://doi.org/10.1146/annurev.ea.10.050182.001103

Macdonald, K. C. (1998). Linkages between faulting, volcanism, hydrothermal activity and segmentation on fast spreading centers. In W. R. Buck, P. T. Delaney, J. A. Karson, & Y. Lagabrielle (Eds.), *Faulting and Magmatism at Mid-Ocean Ridges, Geophysical Monograph Series* (Vol. 106, pp. 27–58). Washington, DC: American Geophysical Union. https://doi.org/10.1029/GM106p0027

Macdonald, K. C., Fox, P. J., Alexander, R. T., Pockalny, R., & Gente, P. (1996). Volcanic growth faults and the origin of Pacific abyssal hills. *Nature*, *380*(6570), 125–129. https://doi.org/10.1038/380125a0

Macdonald, K. C., Fox, P. J., Miller, S., Carbotte, S., Edwards, M. H., Eisen, M., et al. (1992). The East Pacific Rise and its flanks 8–18 N: History of segmentation, propagation and spreading direction based on SeaMARC II and Sea Beam studies. *Marine Geophysical Researches*, *14*(4), 299–344. https://doi.org/10.1007/BF01203621

Maclennan, J., Hulme, T., & Singh, S. C. (2005). Cooling of the lower oceanic crust. *Geology*, *33*(5), 357–366. https://doi.org/10.1130/G21207.1

Mastin, L. G., & Pollard, D. D. (1988). Surface deformation and shallow dike intrusion processes at Inyo Craters, Long Valley, California. *Journal of Geophysical Research*, *93*(B11), 13,221–13,235. https://doi.org/10.1029/JB093iB11p13221

McClinton, T., White, S. M., Colman, A., & Sinton, J. M. (2013). Reconstructing lava flow emplacement processes at the hot spot-affected Galápagos Spreading Center, 95 W and 92 W. *Geochemistry, Geophysics, Geosystems*, *14*, 2731–2756. https://doi.org/10.1002/ggge.20157

Mitchell, N. C., Tivey, M. A., & Gente, P. (2000). Seafloor slopes at mid-ocean ridges from submersible observations and implications for interpreting geology from seafloor topography. *Earth and Planetary Science Letters*, *183*(3), 543–555. https://doi.org/10.1016/S0012-821X(00)00270-3-4

Mougel, B., Agranier, A., Hemond, C., & Gente, P. (2014). A highly unradiogenic lead isotopic signature revealed by volcanic rocks from the East Pacific Rise. *Nature Communications*, *5*(1). https://doi.org/10.1038/ncomms5474

Mougel, B., Moreira, M., & Agranier, A. (2015). A "high 4He/3He" mantle material detected under the East Pacific Rise (15°4′N). *Geophysical Research Letters*, *42*, 1375–1383. https://doi.org/10.1002/2014GL062921

Perfit, M. R., & Chadwick, W. W. (1998). Magmatism at mid-ocean ridges; constraints from volcanological and geochemical investigations. *Geophysical Monograph*, *106*, 59–115. https://doi.org/10.1029/GM106p0059

Pollard, D. D., Delaney, P. T., Duffield, W. A., Endo, E. T., & Okamura, A. T. (1983). Surface deformation in volcanic rift zones. *Tectonophysics*, *19*(1–4), 541–584. https://doi.org/10.1016/B978-0-444-42198-2.50036-5

Ramsey, J. M., & Chester, F. M. (2004). Hybrid fracture and the transition from extension fracture to shear fracture. *Nature*, *428*(6978), 63–66. https://doi.org/10.1038/nature02333

Rubin, A. M. (1992). Dike-induced faulting and graben subsidence in volcanic rift zones. *Journal of Geophysical Research*, *97*(B2), 1839–1858. https://doi.org/10.1029/91JB02170

Rubin, A. M., & Pollard, D. D. (1988). Dike-induced faulting in rift zones of Iceland and Afar. *Geology*, *16*(5), 413–417. https://doi.org/10.1130/0091-7613(1988)016<0413:DIFIRZ>2.3.CO;2

Scheirer, D. S., & Macdonald, K. C. (1995). Near-axis seamounts on the flanks of the East Pacific Rise, 8° N to 17° N. *Journal of Geophysical Research*, *100*(B2), 2239–2259. https://doi.org/10.1029/94JB02769

Searle, R. (1984). GLORIA survey of the East Pacific Rise near 3.5 S: Tectonic and volcanic characteristics of a fast spreading mid-ocean rise. *Tectonophysics*, *101*(3–4), 319–344. https://doi.org/10.1016/0040-1951(84)90119-7

Shah, A. K., & Buck, W. R. (2006). The rise and fall of axial highs during ridge jumps. *Journal of Geophysical Research*, *111*, B08101. https://doi.org/10.1029/2005JB003657

Shah, A. K., Cormier, M.-H., Ryan, W. B., Jin, W., Sinton, J., Bergmanis, E., et al. (2003). Episodic dike swarms inferred from near-bottom magnetic anomaly maps at the southern East Pacific Rise. *Journal of Geophysical Research*, *108*(B2), 2097. https://doi.org/10.1029/2001JB000564

Singh, S. C., Collier, J. S., Harding, A. J., Kent, G. M., & Orcutt, J. A. (1999). Seismic evidence for a hydrothermal layer above the solid roof of the axial magma chamber at the southern East Pacific Rise. *Geology*, *27*(3), 219–222. https://doi.org/10.1130/0091-7613(1999)027<0219:SEFAHL>2.3.CO;2

Soule, S. A., Escartin, J., & Fornari, D. J. (2009). A record of eruption and intrusion at a fast spreading ridge axis; axial summit trough of the East Pacific Rise at 9–10°N. *Geochemistry, Geophysics, Geosystems*, *10*, Q10T07. https://doi.org/10.1029/2008GC002354

Soule, S. A., Fornari, D. J., Perfit, M. R., & Rubin, K. H. (2007). New insights into mid-ocean ridge volcanic processes from the 2005–2006 eruption of the East Pacific Rise, 9°46′N–9°56′N. *Geology*, *35*(12), 1079–1082. https://doi.org/10.1130/G23924A.1

Szitkar, F., Dyment, J., Le Saout, M., Honsho, C., & Gente, P. (2016). Dyking at EPR 16° N hypermagmatic ridge segment: Insights from near-seafloor magnetics. *Earth and Planetary Science Letters*, *453*, 288–297. https://doi.org/10.1016/j.epsl.2016.08.020

Vera, E. E., & Diebold, J. B. (1994). Seismic imaging of oceanic layer 2A between 9°30′N and 10°N on the East Pacific Rise from two-ship wide-aperture profiles. *Journal of Geophysical Research*, *99*(B2), 3031–3041. https://doi.org/10.1029/93JB02107

Weiland, C. M., & Macdonald, K. C. (1996). Geophysical study of the East Pacific Rise 15°N–17°N; an unusually robust segment. *Journal of Geophysical Research*, *101*(B9), 20257. https://doi.org/10.1029/96JB01756–20273

White, S. M., Meyer, J. D., Haymon, R. M., Macdonald, K. C., Baker, E. T., & Resing, J. A. (2008). High-resolution surveys along the hot spot–affected Galápagos Spreading Center: 2. Influence of magma supply on volcanic morphology. *Geochemistry, Geophysics, Geosystems*, *9*, Q09004. https://doi.org/10.1029/2008GC002036

Wright, D. J., Haymon, R. M., & Fornari, D. J. (1995). Crustal fissuring and its relationship to magmatic and hydrothermal processes on the East Pacific Rise crest (9°12′ to 54′N). *Journal of Geophysical Research*, *100*(B4), 6097–6120. https://doi.org/10.1029/94JB02876

Wright, D. J., Haymon, R. M., & MacDonald, K. C. (1995). Breaking new ground: Estimates of crack depth along the axial zone of the East Pacific Rise (9°12′–54′N). *Earth and Planetary Science Letters*, *134*(3-4), 441–457. https://doi.org/10.1016/0012-821X(95)00081-M